SNO-STR-96-055
Fitting Optical Constants in SNO Using a Pulsed N_2/Dye Laser

Richard Ford (Queen's)

March 2, 1997

Abstract

This report outlines methods under investigation to enable an ongoing monitoring of the SNO detector optical condition using the pulsed nitrogen dye laser and diffuser ball system. The absorption lengths in the D_2O, acrylic and H_2O are to be determined by extracting NHIT with various time cuts from the cumulative pmt time histograms. Bulk scattering, pmt QE and reflector condition are also to be determined from analysis of time histograms.

1 Introduction

Understanding the optical condition of the SNO detector is critical to the analysis the detector physics. The detector response to electrons, gamma rays and neutrons can only be measured at certain energies and locations and under limited conditions. Since light transmittance to the pmts is function of event position we expect to rely on Monte Carlo modeling for the analysis. Also the detector gain and response could vary unpredictably due to changes in response of the pmts or changes in the detector optical condition. These changes could include varying impurities in the water systems, deposits on the acrylic or pmt reflectors or gain and efficiency drifts in the pmts. All the optical parameters are wavelength dependent so that the Cherenkov spectrum will evolve as the light travels through the detector.

The optical parameters must be determined at several wavelengths so that this extra positional dependence is correctly modeled in the Monte Carlo (SNOMAN).

This report describes on-going work to develop techniques and analysis methods to determine and monitor critical optical parameters. The recent calibration review [4] emphasized the need for such an interim document outlining progress in the development of optical calibration procedures. This report describes how the optical parameters will be monitored by global fits to time histogram data. Another document [1] reports how some of the techniques described here will be used to perform the initial optical characterization of the SNO detector by boot strapping from air-fill data. This is important, as a measurement of the light attenuation and scattering in the acrylic tiles can only be done once during air-fill before they become complicated by covariances with light water and bulk scattering effects.

The report begins by describing the optics of the SNO detector and the uncertainty with which the optical parameters must be determined. We then describe the optical source, how the detector is triggered and the data acquisition using pmt timing histograms. Next we move through the data processing and, finally, we present procedures that are being developed for fitting to extract the optical parameters. As this work is still on-going a complete calibration run-through including global fits to all optical parameters is not yet completed. Issues dealing with the assessment of bulk scattering and the pmt concentrator reflectors are also discussed.

2 Optical Parameters

2.1 Detector Optical Parameters

To completely understand the optical response of the detector we need to be able to determine, at any time, the following optical parameters.

- Attenuation lengths of the D_2O, the acrylic and the H_2O at several wavelengths between 300nm and 450nm. We would want to know these attenuation lengths for each acrylic panel, any across panels variations and the effects of rope grooves and sanded joints[1] The attenuation

[1] As of December 1996, it seems that there likely will not be any sanded joints. All bond areas are now fine polished to aid inspections.

lengths in the water should be known at as many locations as necessary to account for possible non-homogeneous regions.

- Bulk scattering lengths (cross-sections) and the angular distributions of scattering for all detector regions and at several wavelengths.
- The position/angular response of the pmts and relative quantum efficiencies (QE) of all the pmts.
- Detector optical gain response (absolute QE).

In reality it will be impossible determine all of these parameters and distributions. Instead we must determine which parameters are important and how to measure them, and then understand any limitations this imposes on the analysis. The most critical optical parameters are the extinction coefficients (absorption plus scattering) in the detector media and the relative quantum efficiencies. By deploying the light source [2] at certain locations the separate acrylic panels and water regions can be inspected. Cuts on the pmt timing information can be used to separate out scattered and multiple-reflected light. Other sources (eg. ^{16}N) can provide the overall gain figure.

2.2 Parameter Uncertainty Estimates

For the laserball at the centre of the detector the D_2O attenuates the the total integrated light by a factor $e^{-\mu R}$ where R is the inner acrylic radius. For off-centre locations at radius r the attenuation is

$$\frac{I}{I_0} = \frac{1}{2}\int_{-1}^{1} \exp\left(-\mu r\cos\theta - \mu\sqrt{R^2 + (1-\cos^2\theta)}\right)\, d(\cos\theta) \qquad (1)$$

Evaluating this integral for various r one finds that with a D_2O attenuation length of 40m there is up to a 5% increase in light when the source is near the acrylic. If systematic shifts in the energy calibration are to be less than 1% then we want the D_2O extinction coefficient to be determined to an uncertainty of about 20%.

Now the attenuation lengths are wavelength dependent, especially near the UV, so we really want to weight the integral in equation (1) for the Cherenkov spectrum (λ^{-2}) and the pmt quantum efficiency (QE(λ)). In [6] this calculation has being done by averaging over the wavelength spectrum

(see fig 1). One finds that the integral varies most rapidly for the acrylic with the inference that we need to determine the acrylic attenuation to better than 5%. For the D_2O the required uncertainty is better than 20% while for H_2O 25% uncertainty should be sufficient [6].

It is important to note the approximations assumed in [6]. Sheet-to-sheet variations in acrylic attenuation are not included. Reflections and refraction are not included, both of which would tend to increase the light variation, with the refraction effect being dependent on the acrylic attenuation. Also, we probably want to calculate these uncertainty estimates for each wavelength rather than average over the spectrum. Lastly, isotropic light is assumed while Cherenkov light is directional, thus these estimates are only true in the high statistics limits that permit a reasonable directional average for each radius. These calculations need to be performed with more detailed geometry and scattering effects using Monte Carlo (SNOMAN).

We note also that the variation in the integral (1) has the opposite sign between D_2O and acrylic, and the same sign between acrylic and H_2O. Co-variances between parameter uncertainties for the D_2O and acrylic will require care in assessing the detector positional energy dependence. This will not be as bad for co-variances between acrylic and H_2O parameter uncertainties, which is fortunate as it is known that these co-variances will exist due to some degeneracy in the light path distances. Effects due to scattering have the same sign as for acrylic attenuation (opposite to D_2O attenuation).

Measured data for the acrylic light transmission is presented in figure 2. The panel to panel variations are about 10%. In figure 3 I show the distribution of total integrated detectable light for these data for a Cherenkov source at the centre of the vessel. The Cherenkov output is multiplied by the acrylic transmission and the pmt quantum efficiency and integrated from 250nm to 600nm. The variation is about 1-2%, except that there is a tail extending to 5%. This tail is identified with the panels that have distinctly higher cutoffs[2] as seen with the distributions in figure 2.

[2]Although I have not yet tracked down the identify of all the panels, it is believed that the panels in the tail of the distribution with the higher cutoffs are from the first production runs are were used in the AV qualification wall.

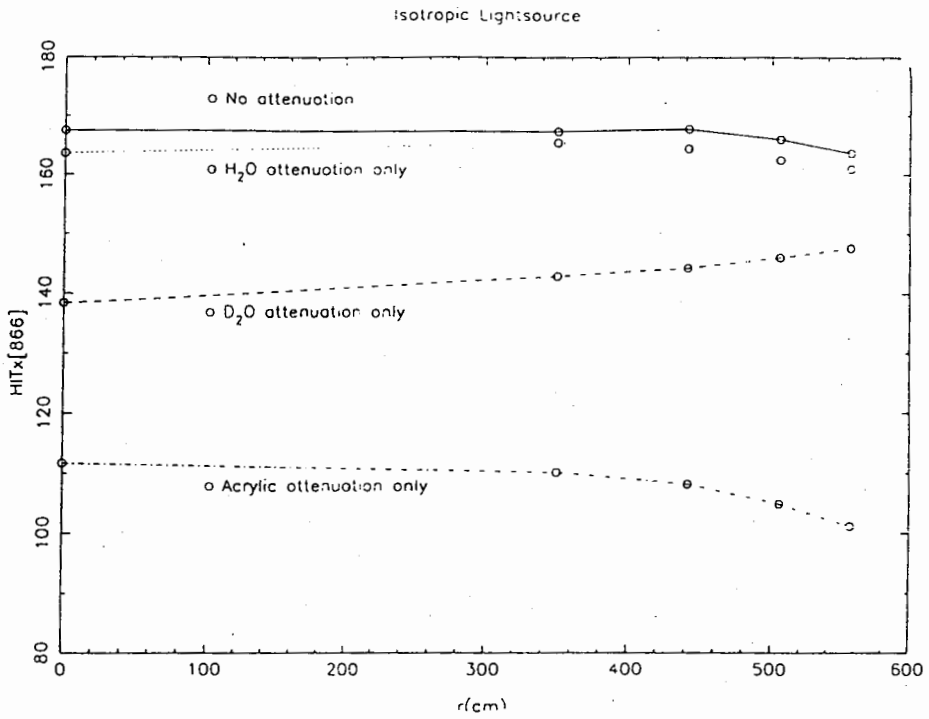

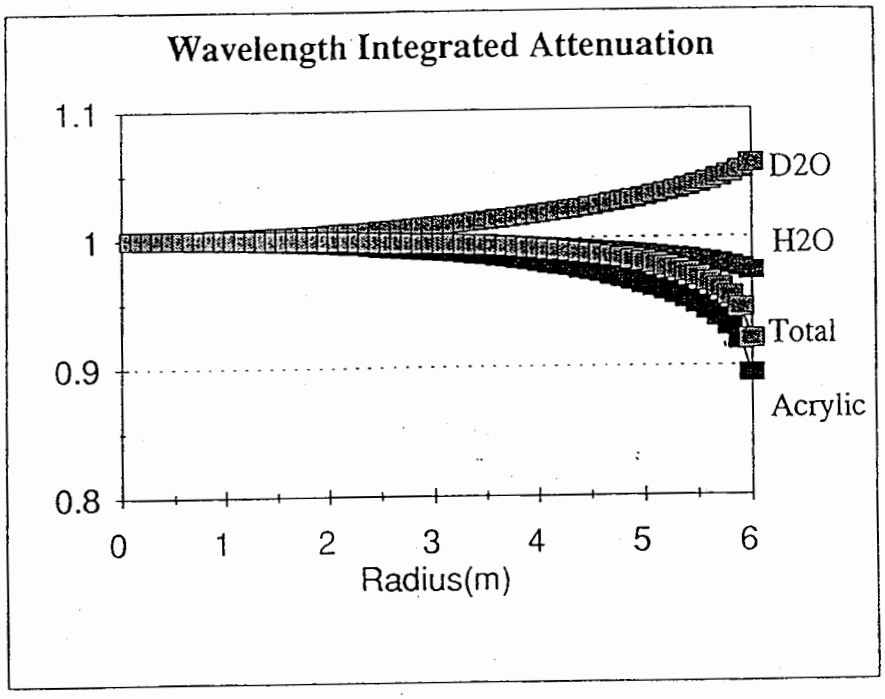

Figure 1: The upper plot is the total attenuation as a function of source radius for an isotropic light source. the secound plot is the wavelength integrated attenuation. From [6] using white book data [7].

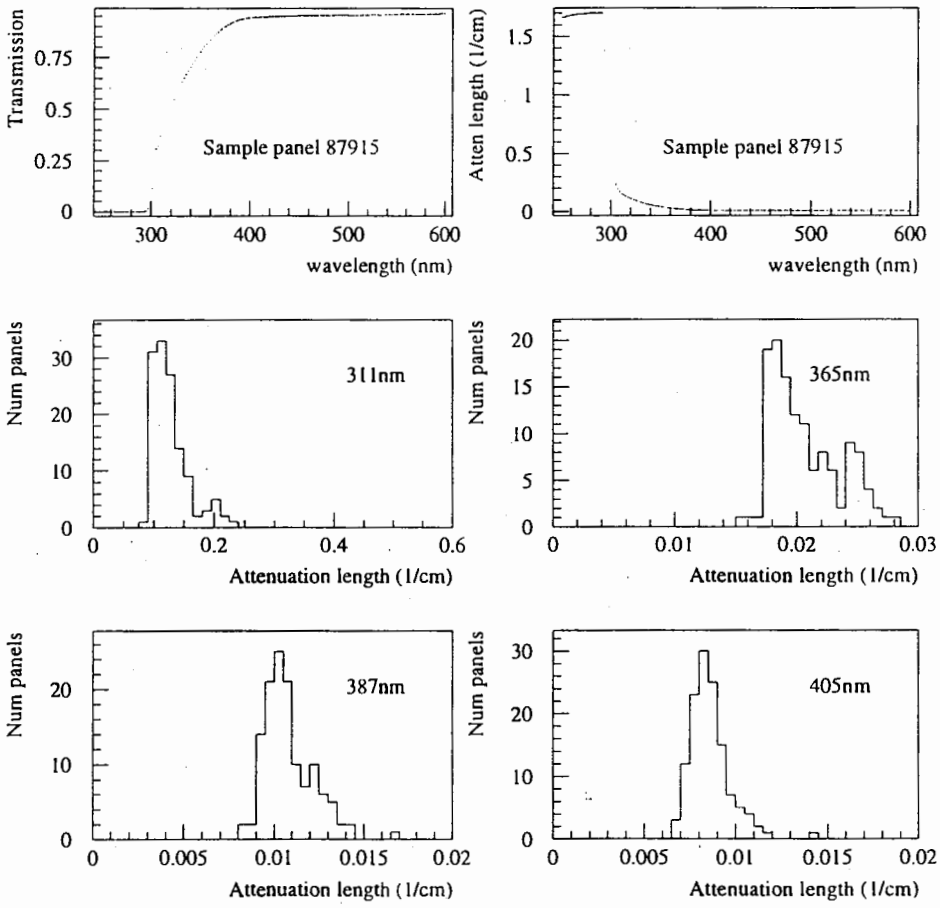

Figure 2: The top two plots show the total transmission and attenuation coefficient as a function of wavelength for a 5.84 cm acrylic panel sample. The remaining plots show the distribution of attenuations for all panels measured at various wavelengths.

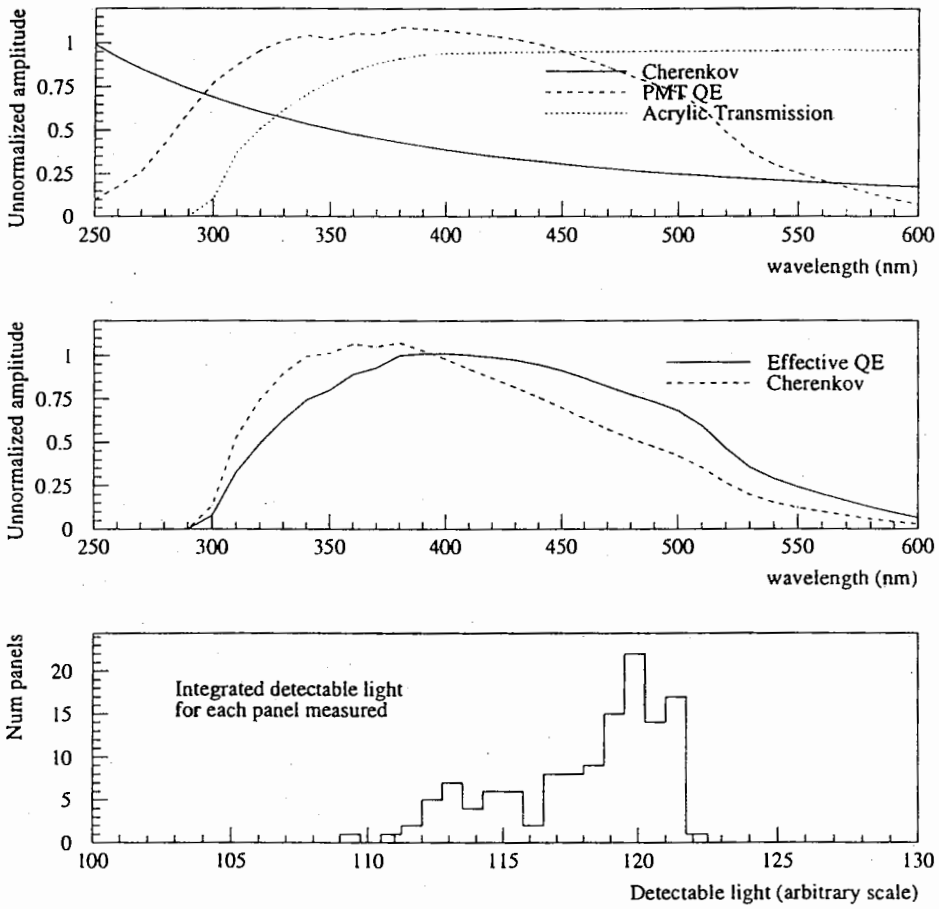

Figure 3: (a) Cherenkov output, pmt response and acrylic transmission as a function of wavelength.
(b) The solid line shows the effective QE by including the AV transmission from the data in the first plot. The dashed line is weighted by the Cherenkov spectrum.
(c) The bottom plot shows the distribution of detectable Cherenkov light by integrating over the data in plot (b) for each of the acrylic measurements. The light scale is arbitrary.

2.3 NHIT Dependence on Optical Parameters

For the laserball at position $\vec{L}_j$, over any time the number of hits in PMT i (position $\vec{P}_i$) due only to the light pulses is given by

$$\begin{aligned} \mathrm{NHIT}_{ij} &= RN_{ij}\Omega_{ij}\epsilon_{ij} \\ &\quad \times \exp\left(-x_{ij}^{\mathrm{D2O}}\lambda^{\mathrm{D2O}} - x_{ij}^{\mathrm{H2O}}\lambda^{\mathrm{H2O}} - \sum_{k=1}^{\mathrm{NPanels=125}} x_{ijk}^{\mathrm{ACR}}\lambda_k^{\mathrm{ACR}}\right) \\ &\quad \times (1 - R_{1ij})(1 - R_{2ij})(1 + S_{ij}) \end{aligned} \tag{2}$$

where R = Number of laserball pulses
N_{ij} = Photons per pulse into unit solid angle (angular distribution of laserball)
Ω_{ij} = Solid angle subtended
ϵ_{ij} = QE including pmt angular response
λ = Extinction coefficient
x_{ij}^{M} = Distance through D_2O or H_2O
x_{ijk}^{ACR} = Distance through acrylic panel k. Note the sum is just for convenience since for a particular i and j only one x_{ijk}^{ACR} is non zero.
R_{mij} = Water-acrylic reflection coefficients
S_{ij} = Hits due to scattered light

In general the extinction coefficients might also depend on $\vec{L}_i$ and $\vec{P}_j$ due to inhomogeneities within the water volumes.

The factor S_{ij} that adds back the detected scattered intensity is a very loose approximation since this does not depend only on the positions $\vec{L}_i$ and $\vec{P}_j$, but it is a complicated function of the entire detector. This is the bane of all optical photometry experiments. The size of the SNO detector makes it unique as a optical instrument, since an analysis of the arrival times of the pmt hits permits the factor S_{ij} to be partially separated out.

Figure (4) contains Monte Carlo histograms of the time between the laser pulse and the time when pmts are hit. The laserball light intensity is low so that all pmt hits result from single photo-electrons (spe). Here the laserball is positioned at the centre of the D_2O, the first histogram is summed over all pmts and the second is typical for a single tube.

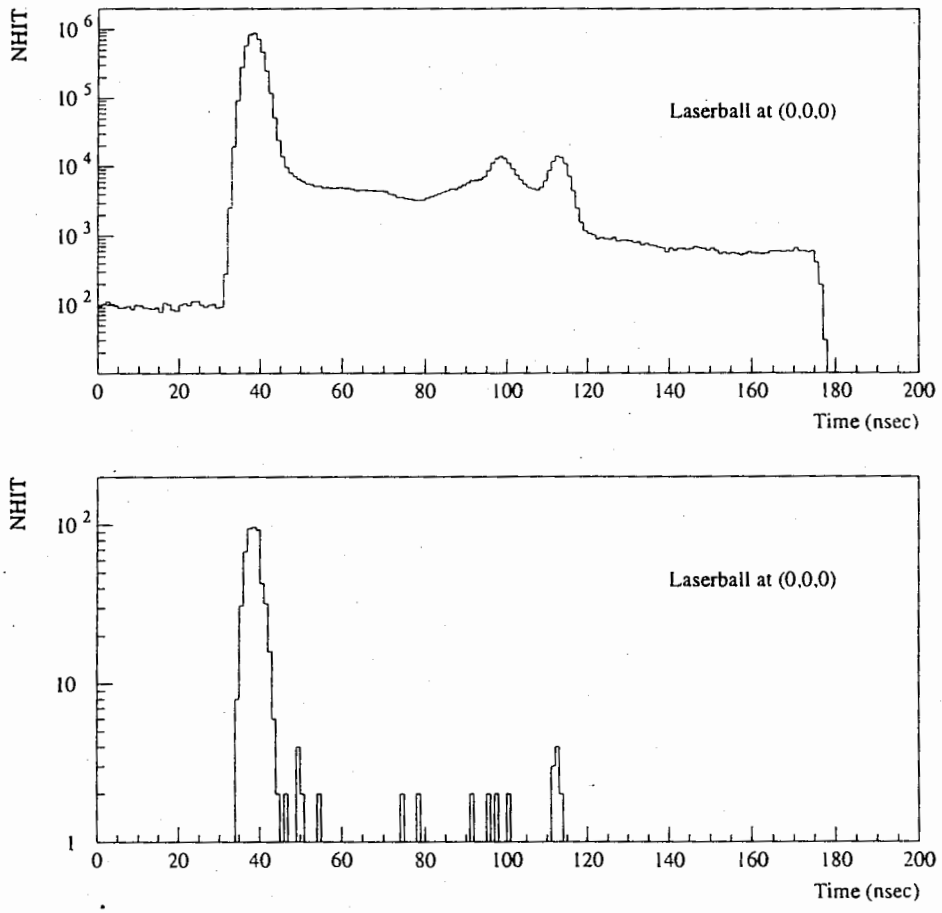

Figure 4: (a) Summed time histogram for laserball at centre of the vessel. (b) Single channel histogram (pmt 0001). Data are from SNOMAN for 10,000 events of 1852 3.21 eV photons with the complete geometry and the 3D pmt model.

The summed histogram clearly shows features attributable to optical processes within the detector, for example reflections and scattering. These different processes can be separated by counting hits within certain time windows within the histogram. These same features are not evident in the single channel histogram, but they are still there, and the number of hits within the same time windows can be counted. In this way, we can decompose time histograms, even with low single channel statistics, such that the statistics will be significant when using all the pmts. The time histograms will be analyzed on this tube-by-tube basis since when the laserball is at any other position the tube times are out of phase and the summed histogram is washed out. Note that due to computer time the histograms in figure 4 contain less than 1/5th of the statistics that will be collected during calibration.

To begin, considering equation (2) one wants to count the photons that arrived on time, ie. no scattering or reflections. This is referred to as the prompt peak, which contains most of the light and is readily observed even in the single channel histogram. Now we need only to decide the integration limits around the peak. This is not a trivial issue since most scattering processes are strongly forward peaked and contribute to the prompt light. This is discussed in detail in sections 6 and 7. After extracting NHIT from all the histograms, and with a knowledge of the detector geometry we are now ready to find the optical parameters.

To get a feel for the scope of the problem one could consider moving the laserball to several locations and collecting NHIT for direct light incident on the PMTs. A linear minimum chi-squared fit might then proceed by considering the log of the above expression and inverting a 128×128 matrix (for 125 acrylic panels plus two extinction coefficients and a gain offset). Unfortunately, drifts in pmt efficiencies, uncertainty in the laserball pattern and covariances between the extinction coefficients make this method all but impossible. Strategies for fitting the optical parameters are discussed in section 6.

3 Hardware and Trigger

3.1 The Laserball

The main optical source is the nitrogen/dye laser with a diffuserball and fibreoptic system (figure 5); see [2] for a complete system description. The diffuserball (called the laserball) can be deployed at various locations within the D_2O volume by the rope manipulator system. The laserball can also be positioned on a single axis by lowering down through the acrylic vessel neck or through the calibration entry ports into the PSUP light water.

The primary laser source is a TEA thyratron triggered N_2 laser producing a 600psec pulse at 337.1nm at a peak power of about 150kW. This primary beam can be delivered directly to the fibre-optic coupling optics, or it can be used to pump one of four available dye-laser units. The selection is made with a fully remote computer controlled movable mirror mechanism.

The dye laser units produce super-radiant incoherent radiation with approximately 500psec pulse width and about a 20nm bandwidth (FWHM). The present choices for the central wavelengths are 365nm, 386nm, 405nm and 420nm. Many other frequencies are possible; requiring the manual interchange of a 5cc dye cuvette. Beam steering optics direct all the dye unit outputs to the same fibre-optic mixer.

The laser output stage consists of two remote independent neutral density filter wheels, fibre coupling stage, mode mixing pipe and PIN diode energy monitors.

The laser light is coupled into a bundle of 22 improved bandwidth, step index high OH silica fibres. This bundle is then cabled with a RG-174U transmission cable using loose irradiated PVC (heat shrink). This cable is then potted with a soft silicone dielectric gel inside a 1/2" OD silicone tubing. This cable tubing (the source umbilical) is wound over an enclosed pulley array (like a block-and-tackle rig) which provides cable storage and tension control. The pulley array device is required due to the complexity of a rotating coupler that would be required by any other cable take-up method.

The fibreoptic umbilical is terminated with a 10cm diameter diffuser ball which serves to distribute light isotropically through the detector. The diffuser consists of foamed glass bubbles mixed into a soft transparent silicone cured within a quartz glass boiling flask. The neck plug contains a fibreoptic positioning guide tube and also houses a miniature monitoring pmt (Ham-

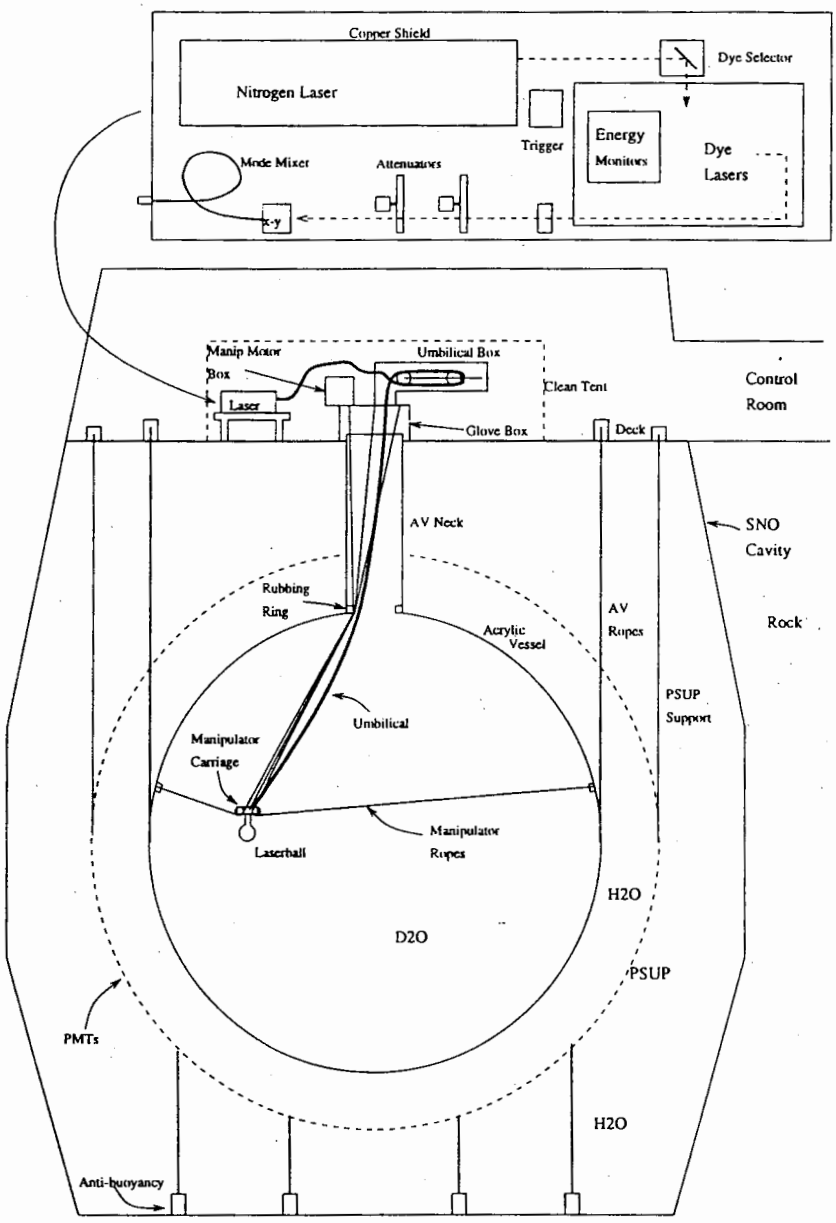

Figure 5: Schematic of the N_2 laser calibration system.

mamatsu R5600). The RG-174U cable serves as the HV and the signal line for the pmt. The fibre-optic guide tube allows the umbilical cable to be detached from the laserball and reconnected without adjustment to the light output pattern. Figure (6) show a sample laserball light pattern; the plot shows the light intensity over the polar angle at a fixed azimuth orientation.

3.2 Trigger and Histograms

The optical calibration requires pmt hit time histograms as described in section 2.3. The required time is the time difference between the laser light pulse and and the arrival time of the pmt pulse at the front-end card (FEC) after correcting for relative timing offsets. Remaining time offsets are constant and arbitrary, depending on cable lengths and speed of the trigger logic etc.

The laser system light pulse fires a fast diode trigger that runs through a cable delay to a special FEC. The special FEC starts it's own TAC and causes a global detector trigger to be set on the next 50MHz clock signal. The laser trigger delay will be set so that most of the approximately 250nsec trigger window is utilized. Note that there should be no noticeable effect due to latching the trigger on to the 50MHz GPS clock since running up the laser trigger TAC will compensate for the extra time on the pmt TACs.[3] This can be verified by collecting data in event mode where all the TAC amplitudes are written to tape.

It is planned for the DAQ to be able to collect single channel histograms in one of two modes: event mode and histogram mode.

In event mode the DAQ event builder writes the laser events to tape exactly like a neutrino or other event. The event is identified as a laserball event as the global trigger was fired from the special FEC. Histograms are then filled in SNOMAN using a processor called the data filter. There are also several pulses from energy monitors in the laser system that go to other special FECs. Since these pulses are quite slow the DAQ will write them out some time later as a separate event record. Other computers, for example the calibration computer, can query the DAQ for the cumulative histogram of these monitor pulses.

In histogram mode the time differences are stored in histograms on the

[3]This is called the synchronous trigger. Although an asynchonous trigger has been extensively discussed it is not known at this time if it will be implemented.

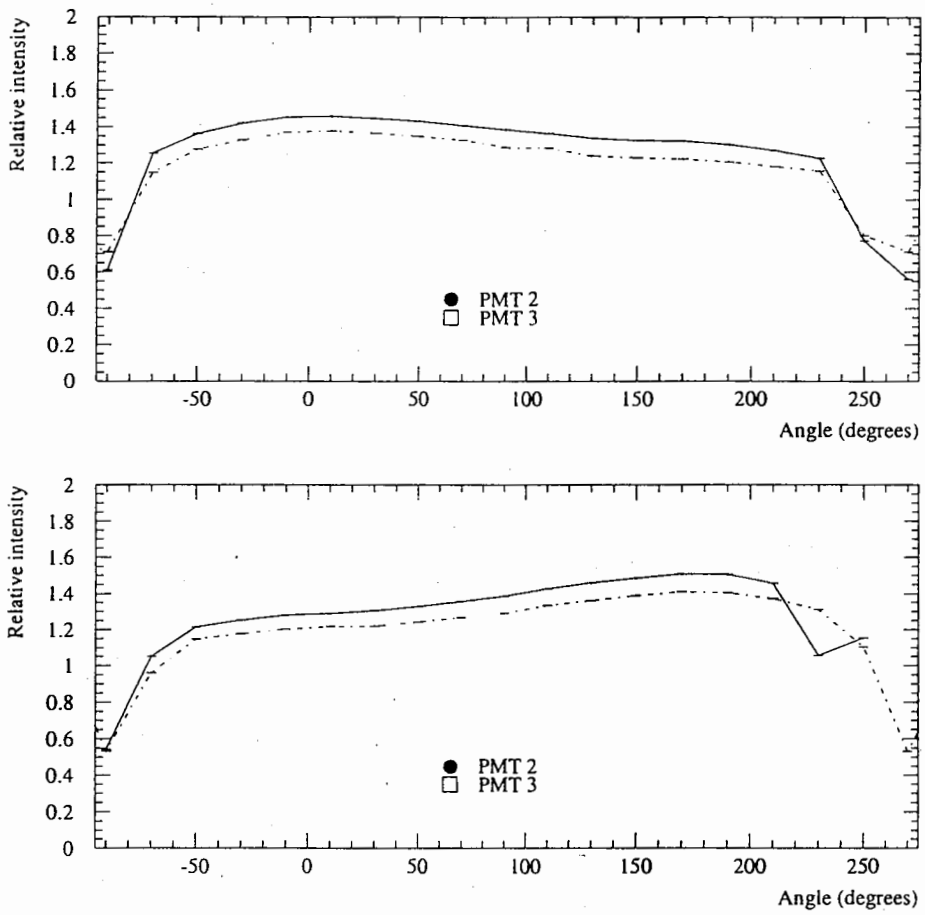

Figure 6: Single axis laserball scans with two opposite facing pmts with pulse heights normalized to the laserball internal pmt pulseheight. Angles for pmt 3 are displaced 180 degrees. The fibre-optic position in the laserball was adjusted between the two scans to demonstrate how the isotropy can be adjusted. (a) Scan before fibre adjustment, (b) scan after adjustment.

front end embedded CPUs. The laser monitor pulses are histogrammed by the DAQ. Events due to triggers from the laser FEC are not build and written to tape. At this time it is not specified whether the histograms will be 1D or 2D (time and charge), or whether the two TACs and the low and high gain integrators will be separately histogrammed. Note that in this mode the detector treats all other triggers in the usual way. One consequence of this is that the detector will retrigger on late laser light. There may be implemented a lockout on the NHIT trigger following the laser pulse (eg. 400 nsec) to prevent these re-triggers. If we wanted to collect this late light in a useful way the laser FEC would have to provide a retrigger after a set time delay (eg. $\sim$ 200 nsec).

4 Distances in Media

To fit an expression for NHIT with the laserball (eg. equation 2) requires calculation of the distances through each medium for every pmt and laserball position. While this sounds straight forward there are subtleties involved. One cannot simply take the straight line distances between the source and the pmt because this would always reduce the distance in the acrylic (due to refraction), resulting in a bad fit and a large error in the acrylic attenuation.

Even with simple geometry (an acrylic sphere) an analytic solution for the path length is difficult. A reasonable approximation for small angles is to assume a path in the D_2O toward the pmt, refract through the acrylic and then compromise the exit angle by simply joining to the pmt. A proper solution can be found by iteration, where subsequent direction cosines are estimated from the closest approach to a target pmt. The path distances in each media are recorded after convergence to the target pmt.

The iteration method is able to cope with complex geometry but it is slow and will fail to converge for (real) pathological circumstances. The approximation is quicker and could include correction factors based on the iterated calculation. For real time optical calibration it would be best to have all the distances pre-calculated in a look-up table for 10 to 20 pre-determined source locations. This would not be unreasonable as the optical calibration would be executed by running the laserball at set locations within the detector.

Another item to consider is what co-ordinate one takes for the location

of the pmt. What is required is the location that the photon entered the pmt concentrator bucket. Of course it is impossible to know this information and the hits in the cumulative histogram would have occurred all over the photo-cathode surface. We want a single target point that well represents the pmt in an average sense. This average must correctly weight the detection probabilities so that the resulting path distances are representative.

The problem can be significant for finding the correct path distance through the acrylic; it is much less important for the D_2O and H_2O distances. Consider figure (7), if we take the given pmt position (eg. from the LBL data) as the path target then there is an asymmetry in the detection probability around this point. This would cause a systematic under-estimate of the acrylic path length. A better estimate for the average target point is a point on the pmt axis about one centimeter outside the opening of the reflector bucket. The extra centimeter should be added back to calculate the solid angle correctly and an extra 10 centimeters should be added to estimate the H_2O path distance.

Really what we want is an average path through the acrylic weighted by the probability of a pmt hit, ie.

$$\overline{x}_{\rm acr} = \frac{1}{\Omega_0} \int x_{\rm acr}(\theta, \phi) P(\theta, \phi)\, d\Omega \tag{3}$$

where $P(\theta, \phi)$ is the probability of the pmt detecting a hit for a given path, $x_{\rm acr}(\theta, \phi)$ is the corresponding path length through the acrylic and Ω_0 is the projected pmt solid angle. The SNOMAN Monte Carlo is actually well suited for evaluating such an integral. By running many events with an isotropic source we can weight $x_{\rm acr}$ with the number of hits. This calculation would have to be done off-line requiring the look-up table method for path distances in the optical parameter fitting.

A problem with optical calibration is that for positions in the D_2O the path lengths through the acrylic and H_2O are highly correlated, as seen in figure 8. Thus it takes high statistics and positions near the acrylic to effectively separate the H_2O and the acrylic attenuations. This degeneracy breaks only at the highest angles into the acrylic, precisely where the errors in the calculated distances will be greatest.

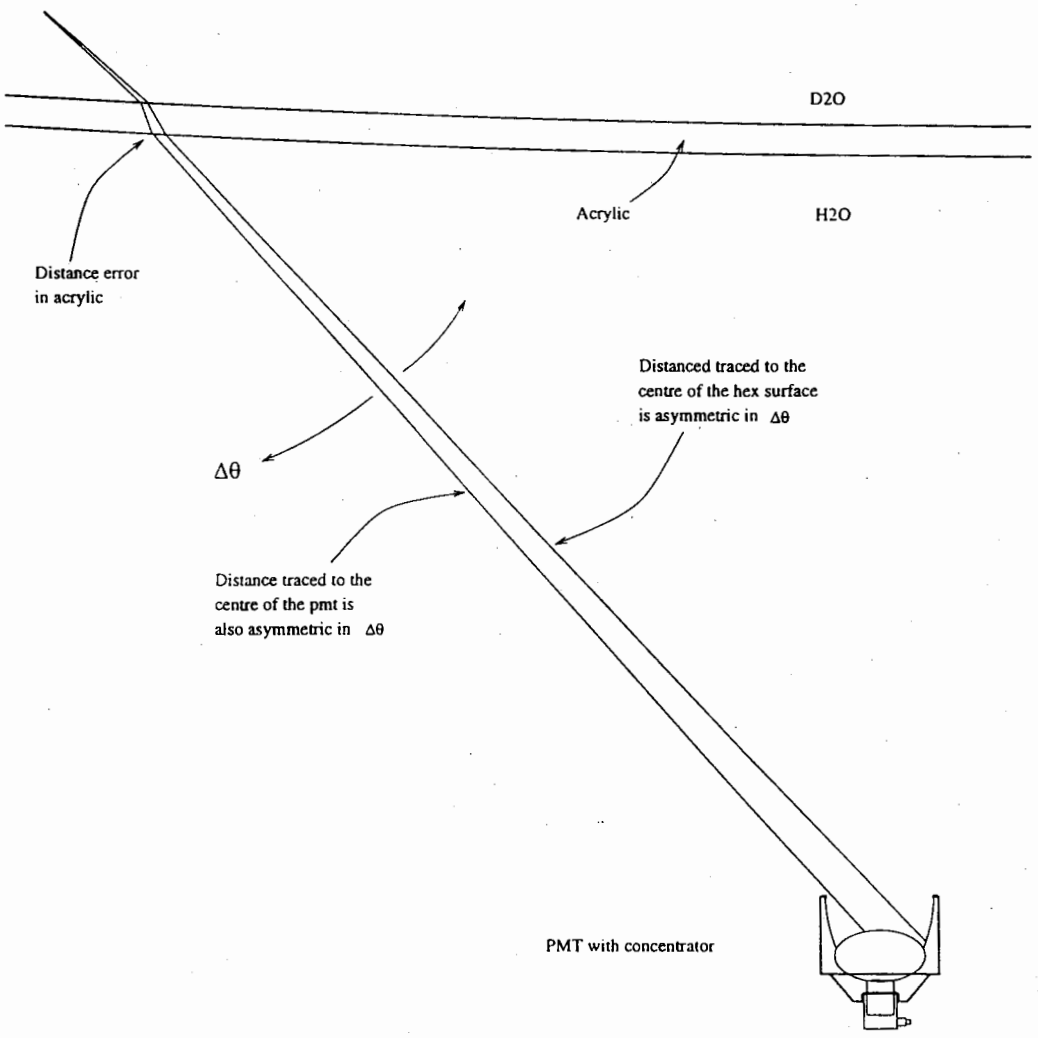

Figure 7: Defining the target distance to a pmt.

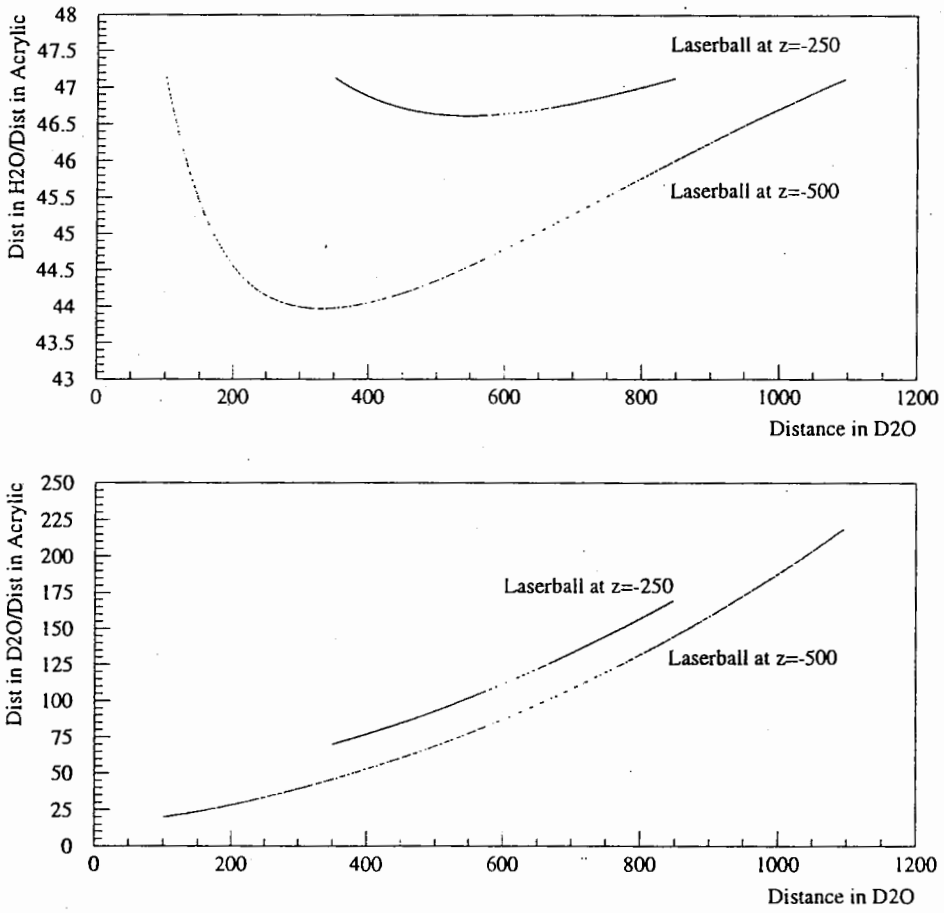

Figure 8: (a) Ratio of the distance in H_2O to the distance in acrylic as a function of path length in the D_2O for two laserball positions. This shows that the path lengths are highly correlated so that a determination of the H_2O attenuation is strongly coupled to the acrylic attenuation. (b) Ratio of the distance in D_2O to the distance in acrylic as a function of path length in the D_2O for two laserball positions. These attenuations are not strongly coupled.

5 The Time Histogram

In this section we examine closely the pmt time histograms and discuss how optical processes within the detector are manifest in the time distribution. We will then discuss how the various cuts are made on the time histograms to extract NHIT to fit for the optical parameters.

The time histogram (eg. figure 4 and 10a) contains peaks due to the prompt laser pulse and any other focussed reflections. The remainder of the histogram is due to bulk scattering and unfocussed reflections. As discussed in section 2.3, the cumulative histogram would be smeared out for all other laserball positions. However, this histogram is still relevant as the similar features could be found in the individual pmt histograms with much higher statistics.

The time histograms are characterized by a large prompt peak with secondary peaks and scattering tails at later times. The largest secondary peak is found at 113.3 nsec which corresponds to the expected three radius transit time. The two earlier peaks are also due to pmt reflections, and are the result of the photocathode-reflector response which is discussed in section 8. SNOMAN and the Queen's Monte Carlo both include only Rayleigh scattering which produces the terraced features in the histogram. See figure (23) in section 7.1 where dipole scattering is discussed. Secondary scattering and reflection hits run down into the background noise hits before the TAC timeout. The time histogram patterns for some different combinations of scattering and reflections can be studied from figure 9 where QMC data is presented with several conditional cuts.

Some individual pmt time histograms are shown in figure (10) for the laserball at several positions. Histogram (c) for PMT 9365 is an example of a lensing phenomena which is quite rare but it is expected from the detector geometry and must not be mistaken for prompt light. Histogram (d) shows a common problem with a light source in the H_2O where broad peaks from reflections off the acrylic dominates the spectrum. Other effects due to pmt pre-pulsing and after pulsing are not yet included in the Monte Carlo.

The optical analysis proceeds by locating the prompt peak with a sliding window algorithm. The algorithm finds the window location with the largest NHIT and checks if the peak is reasonably distinguished and close to the expected prompt time. Alternate peaks are inspected until the prompt light is identified. The peak is integrated to find NHIT and the centroid and

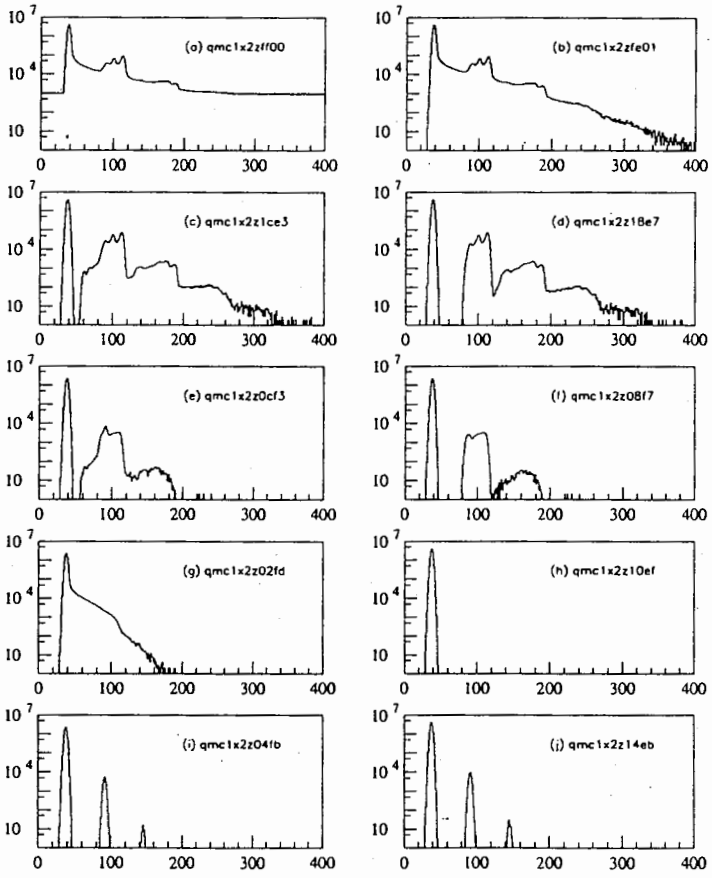

Figure 9: (a) All hits (b) No noise (c) No noise or scattering (d) No noise, scattering or AV reflections (e) No noise, scattering or omega reflections (f) Photocathode reflections only (g) Scattering only (h) Omega reflections only (i) AV reflections only (j) AV and omega reflections only

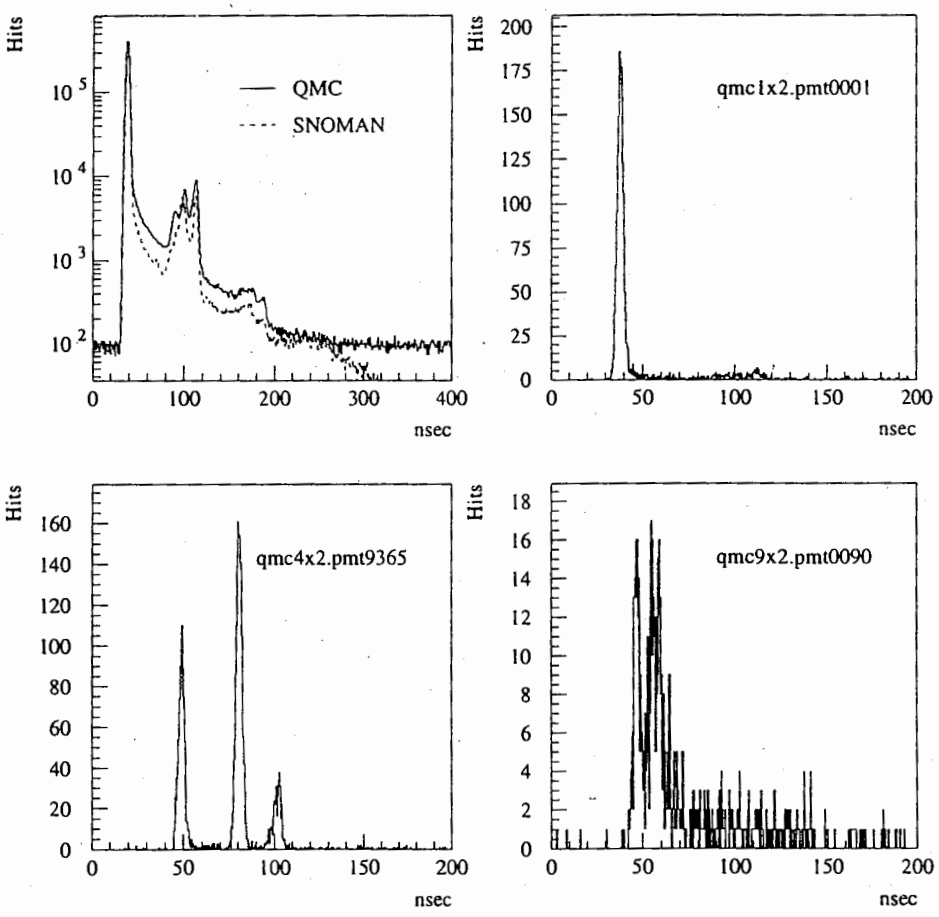

Figure 10: a) Summed time histograms for SNOMAN and QMC
b) PMT 1 for laserball at (0,0,0)
c) PMT 9365 for laserball at (0,0,-500)
d) PMT 90 for laserball in H_2O at (650,0,374)

widths are calculated from the distribution moments. The window width is set empirically at 7 nsec (see figure 15) due to the scattering tail on the late side of the prompt light. A possible refinement here is to double the integral of a half window on the early side of the peak centroid.

Other intervals relative to the prompt peak are then analyzed. A 30 nsec window following the prompt time is integrated to find the scattering contribution. The scattering component is characterized by the slope at the centre of the 30 nsec window; this is discussed further in section 7. Other time windows can also be integrated at this time, for example to examine the pmt reflectors using the 35° image ring (see section 8).

A remaining consideration is the adjustment of light source intensity to maintain single-photoelectron (spe) pmt response. At low intensities the photoelectron multiplicity is a Poisson distribution $P(n, \mu)$ with a mean detected light intensity μ. If the laser is pulsing at rate R then in time t the number of pmt hits is

$$\text{NHIT} = Rt\,(1 - P(0, \mu)) = Rt\left(1 - e^{-\mu}\right) \tag{4}$$

To keep the probability of two or more photoelectrons to less than 1% would require that the mean event probability be less than 2%-3% everywhere. This would be impractical given the large variation in pmt solid angles when moving the laserball, and would result in very low statistics. Instead we choose the intensity so that most of the pmts are at spe intensity and make the correction

$$\text{Eff. Hits} = -Rt \times \log\left(1 - \frac{\text{NHIT}}{Rt}\right) \tag{5}$$

where Rt is the total number of laser flashes.

Higher photoelectron multiplicities will also distort the time spectrum and so it is important to understand this quantitatively. The time spectrum distortion is due to the discriminator firing on the leading edge of the pulse which results from the first photoelectron. The timing spectrum can be calculated by multiple convolution with a Gaussian for each photoelectron with a cut-off at the time for the first photoelectron. These spectra can then be summed with Poisson weightings. This calculation is easiest to perform as a Monte Carlo, since the first photoelectron time selection imposes awkward cut-offs on the integrals.

Figure 11 shows the results of such a calculation assuming a Gaussian shape with a sigma of 0.9 nsec for the laserball pulse and a pmt transit

time spread of 1.4 nsec. In the first plot the abscissa is the mean light intensity which is linearly related to the laserball output and equal to NHIT probability in the low intensity limit. In the second plot the abscissa is NHIT probability which would be just NHIT/Rt. The first line plotted is the ratio of the mean intensity to NHIT probability which shows how NHIT varies with multiple photoelectrons. The second line is the centroid value of the time peak (with an arbitrary 3 nsec offset) which is seen to shift to earlier times with increasing NHIT. From the third line we see that the sigma also decreases but only very slowly. From linear fits to the plots the following approximate adjustments can be used for NHIT probabilities up to 50%

$$t \longrightarrow t - 0.66 \times \frac{\text{NHIT}}{\text{Laser pulses}} \tag{6}$$

$$\sigma \longrightarrow \sigma - 0.042 \times \frac{\text{NHIT}}{\text{Laser pulses}} \tag{7}$$

A spline to the data can be used for larger probabilities.

Note that the timing issues discussed here are in addition to the electronics Q versus T walk corrections. Since larger pulses will cross the discriminator threshold at earlier times there is a pulse-to-pulse systematic charge dependent shift. This correction is made by the crate level computers using look-up maps before the data is histogrammed or recorded to tape.

6 Fitting for Extinctions

6.1 D2O Attenuation

Although we expect to calculate posterior probabilities simultaneously from the global likelihood, it is a good idea to first start by just finding the attenuations separately. For the D_2O a straight line fit for the attenuation ought to work well since large variations in the D_2O path length can be achieved between source locations with small variation in other parameters (eg PMT angles). In particular one can think of the special case where the PMTs below the south pole view the laserball at several locations on axis.

The logarithm of prompt NHIT, with solid angle and rate corrections is plotted in figure 12 for 105 PMTs that are viewed through the southpole panel at five on-axis laserball positions. A straight line fit yields the extinction coefficient (-0.000297 cm^{-1} or 34m) and a gain offset which is quite

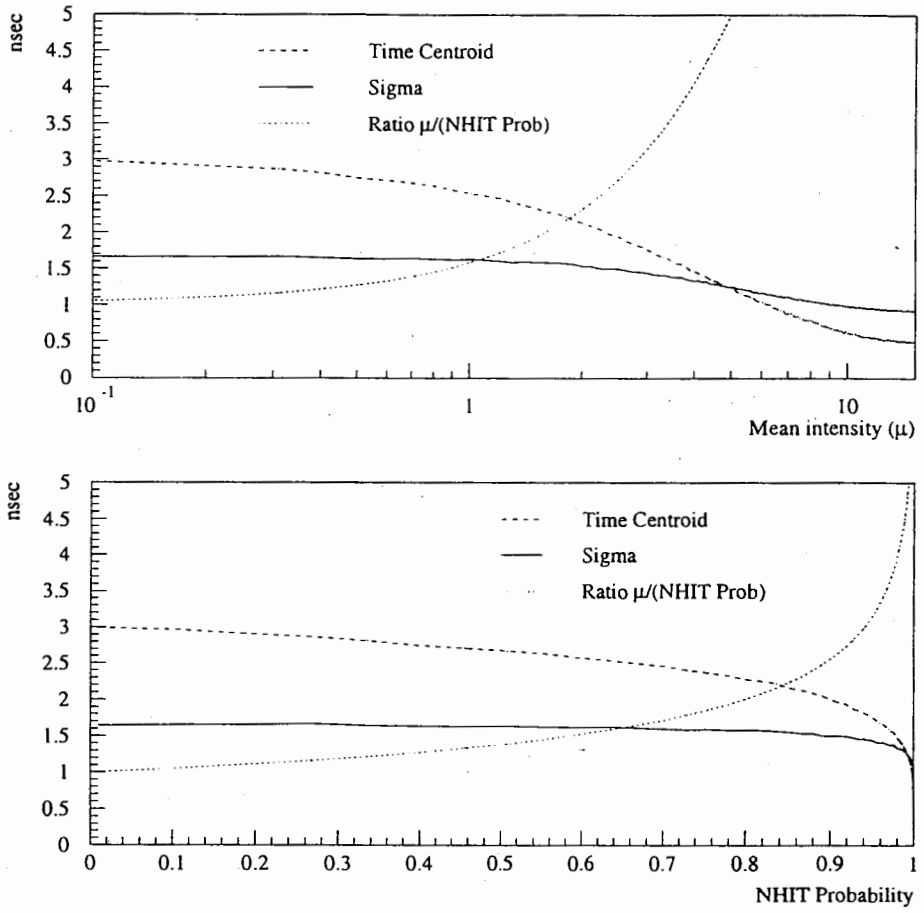

Figure 11: Plot of time centroid shift and sigma versus mean light and NHIT Probability for a single pmt (see text).

arbitrary as the absolute QE is unknown (QMC Monte Carlo input value for the extinction coefficient is -0.00031 cm^{-1}).

Fitting with all the pmts offers much better statistics, but does introduce a dependence on other estimated parameters, ie. the acrylic attenuation and the angular pmt response. Figures 13 and 14 present results for QMC (-0.000286 cm^{-1}) and SNOMAN (-0.000404 cm^{-1}, SNOMAN Monte Carlo input value is -0.000407 cm^{-1}). The upper plots show a two dimensional chi-squared surface, with it's contour map, while the lower plot shows the best straight fit through the data.

Using this data I now return to the issue of choosing the width of the integration window for the time histograms. The above fit was repeated with NHIT extracted using varying integration window widths. The result is shown in figure 15; empirically 7 nsec is a reasonable choice for the integration width.

6.2 Acrylic Attenuation

Similar fits for the attenuation in the acrylic are shown in figures 16 and 17. Before fitting cuts are made on those pmts with large incidence angles ($> 40°$) since this light must have been scattered and because the angular response is less certain at larger angles. Cuts are made also for optical paths with a large distance in the acrylic since these path distances and directions are less certain. In future a statistical weighting scheme will be developed for these data since a large proportion of the hits occur at large incidence angles. Fit results are -0.0201 cm^{-1} in QMC and -0.0182 cm^{-1} in SNOMAN for input value of -0.02 cm^{-1}.

These fits to the acrylic attenuation draw attention to the problem of sensitivity to the pmt angular response. Figures 18, 19 and 20 show how most of the pmt hits always come from the pmts for which the incident angle for the direct line of sight is the largest. This means that most of the statistical weight is placed on high incidence angle hits, so that any uncertainty in the pmt angular response will cause errors in the fitted attenuations. The pmt angular response has been measured and is approximately flat out to 40° [9]. To investigate how the complicated optics of SNO may distort the large angle response I have reconstructed the effective pmt response from SNOMAN Monte Carlo data. I reconstruct the response by correcting NHIT with the known attenuations and solid angles. The reconstructed response

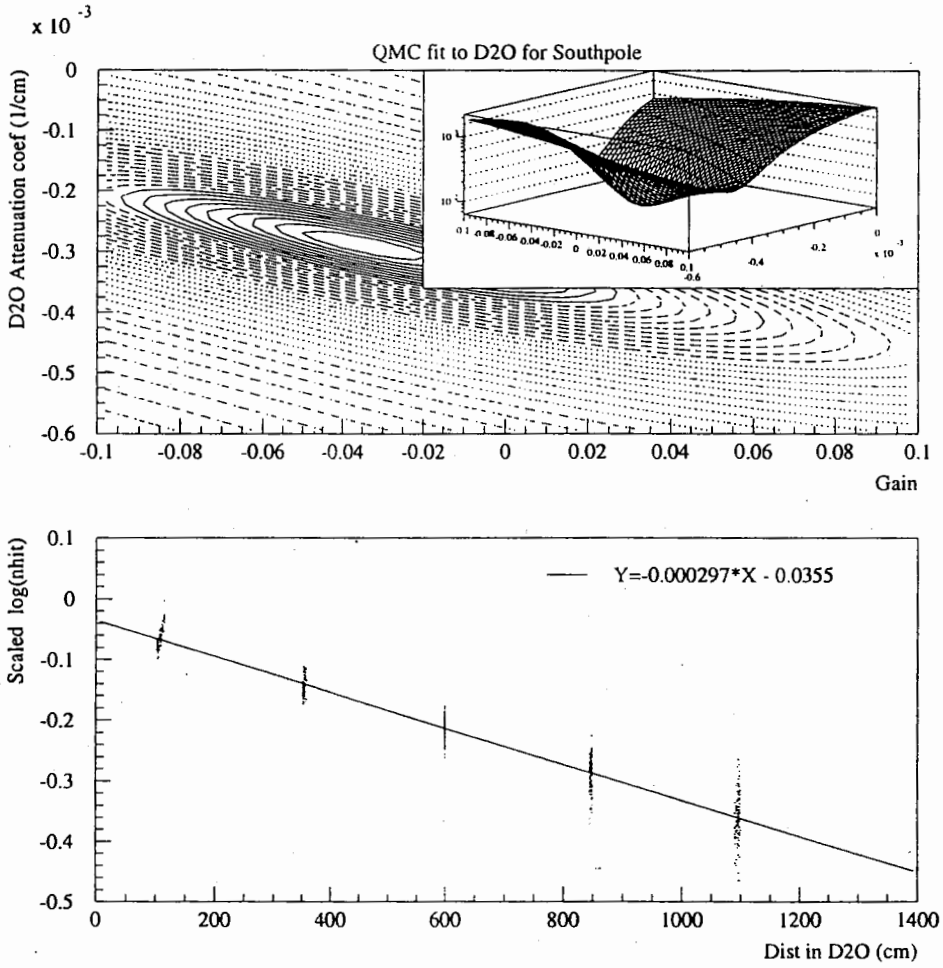

Figure 12: Fit to log(NHIT) and distance in the D_2O from QMC data with pmts below the 111 panel (southpole) for the laserball at 5 positions on axis within the D_2O. Fit yields an extinction coefficient of -0.000297 (1/cm) or 34m. The upper plot shows the Chi-squared surface.

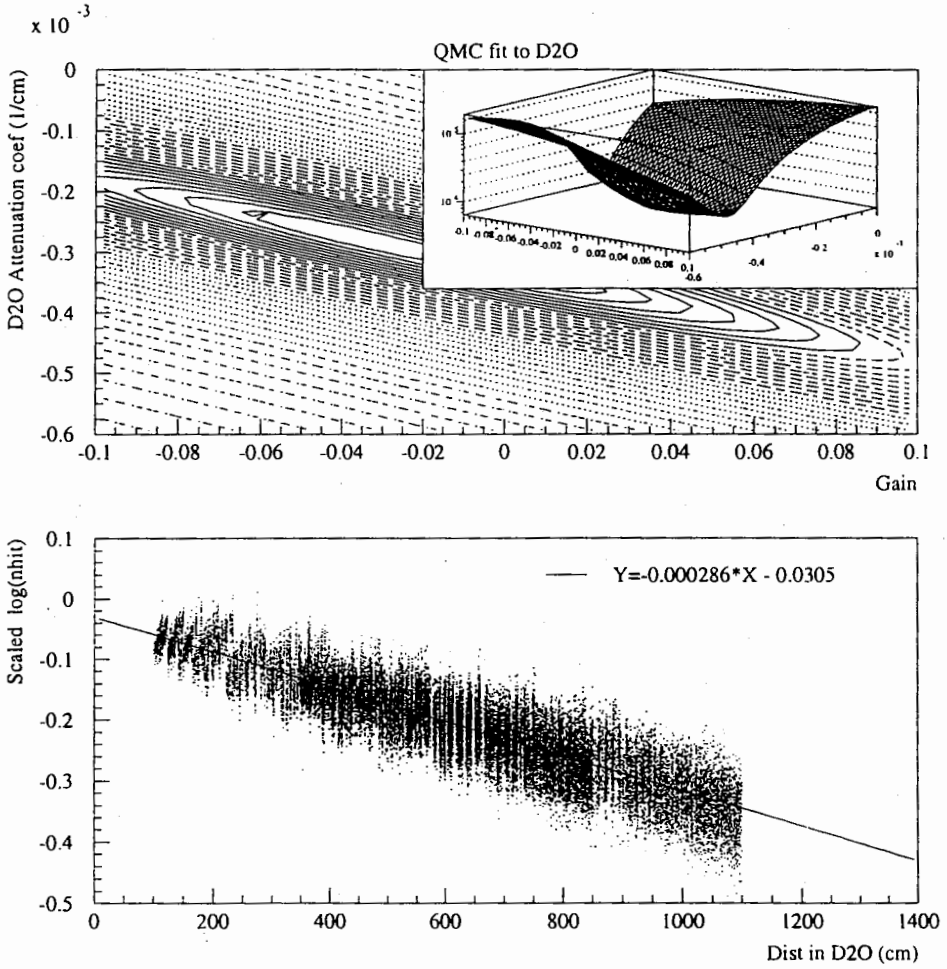

Figure 13: Fit to log(NHIT) and distance in the D_2O from QMC data for the laserball at 5 positions on axis within the D_2O. Fit yields an extinction coefficient of -0.000286 (1/cm) or 35m. The upper plot shows the Chi-squared surface.

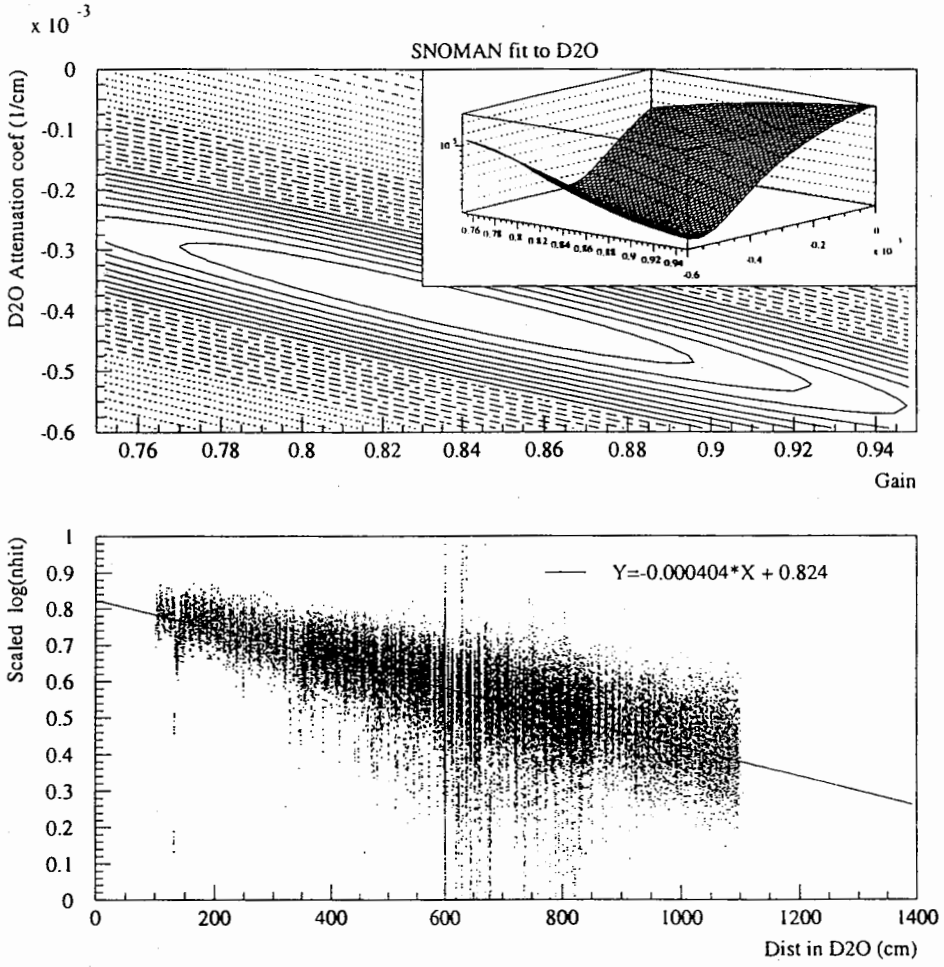

Figure 14: Fit to log(NHIT) and distance in the D_2O from SNOMAN data for the laserball at 5 positions on axis within the D_2O. Fit yields an extinction coefficient of -0.000404 (1/cm) or 25m. The upper plot shows the Chi-squared surface.

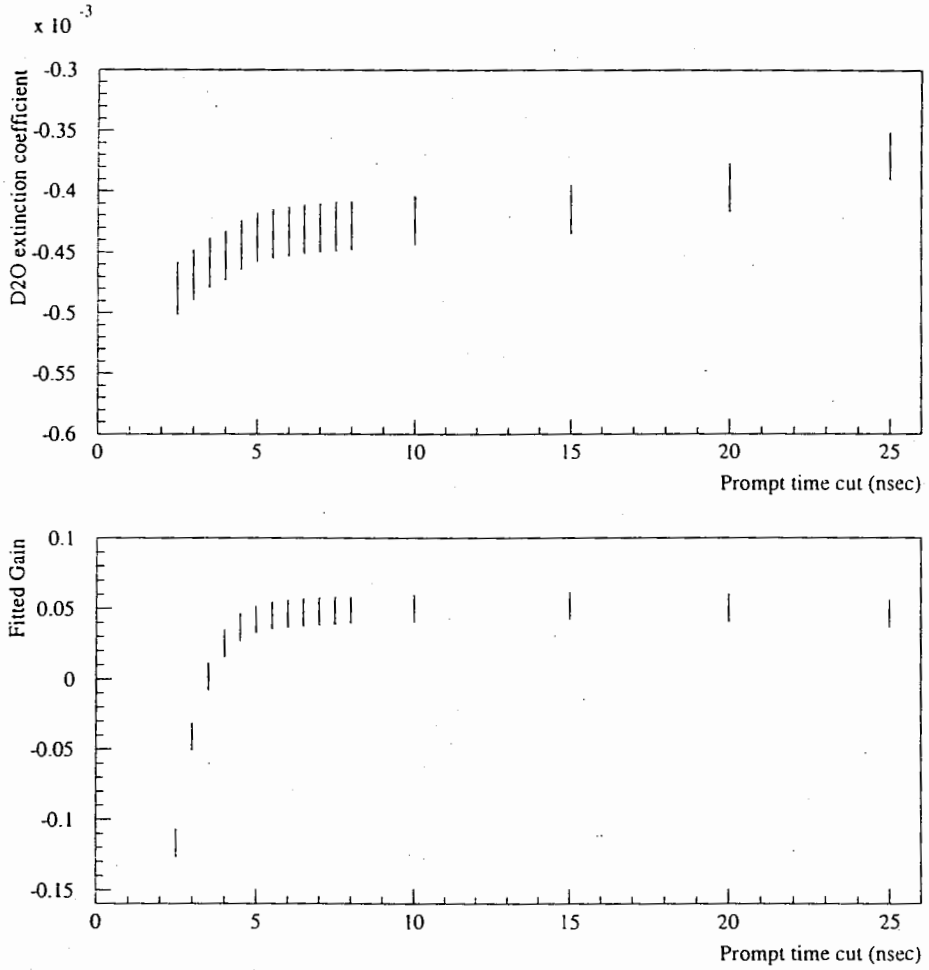

Figure 15: Fitted D_2O attenuation and gain versus window width using SNOMAN data for southpole pmts. A window width of 7 nsec appears to be reasonable choice.

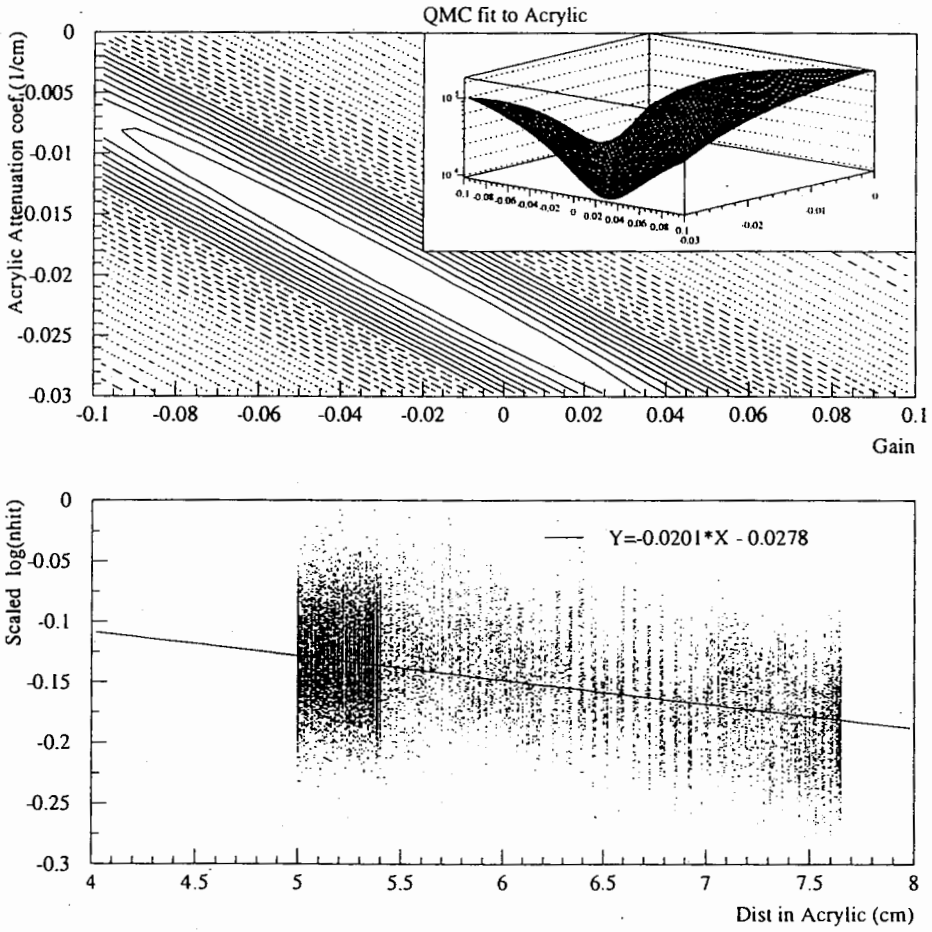

Figure 16: Fit to log(NHIT) and distance in the Acrylic from QMC data for the laserball at 5 positions on axis within the D_2O. Fit yields an extinction coefficient of -0.0201 (1/cm) or 50cm. The upper plot shows the Chi-squared surface.

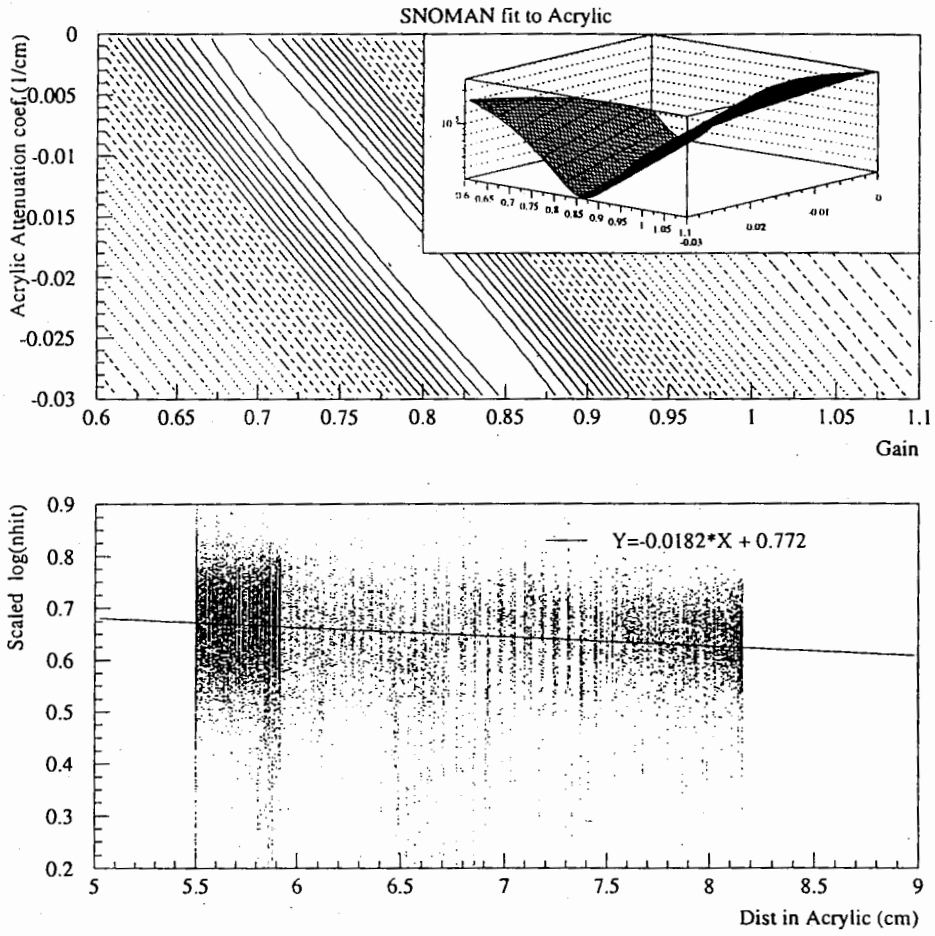

Figure 17: Fit to log(NHIT) and distance in the Acrylic from SNOMAN data for the laserball at 5 positions on axis within the D_2O. Fit yields an extinction coefficient of -0.0182 (1/cm) or 55cm. The upper plot shows the Chi-squared surface.

(figures 19 and 20) is nearly flat, with a slight downward slope, but also shows distortions, for example at 25°-30° with the laserball at (0,0,-500). Sensitivity to this distortions can be reduced by using a weighting inversely proportional to the pmt geometric distribution for each laserball position. An alternative is to model the pmt response as $y = \alpha + \beta\theta$ where α is absorbed in the overall gain and the slope parameter β is a free parameter fitted with the data (the same for all pmts).

6.3 Simultaneous Fit

A multi-dimensional linear function (equation 2) is minimized for three parameters, the D_2O and acrylic attenuations and a gain figure. The chi-squared surfaces are shown in figures 21 and 22 for QMC and SNOMAN data. The best value for QMC are -0.000284 cm^{-1} for D_2O and -0.0172 cm^{-1} for acrylic. The input values are -0.00031 cm^{-1} and -0.02 cm^{-1}. For SNOMAN the fitted values are -0.000406 cm^{-1} for D_2O and -0.0280 cm^{-1} for acrylic, while the input values are -0.000407 cm^{-1} and -0.02 cm^{-1}.

7 Fitting for Scattering

Light scattering in the SNO detector is a difficult phenomenon to measure as it can have many causes and effects. Scattering can be intrinsic to the material, like Raleigh scattering, or can be due to coherent or incoherent scattering and reflections off particulate matter ranging in size from nanometers to tens of microns. Due to the large size of the SNO detector, even in infinitely clean water, scattering is a common process with over 10% of detected light having been scattered. Scattering can change the resolution and gain of the detector. Fitters that attempt to identify events by hit pattern recognition might be particularly sensitive to scattering distributions that are different from any training sets used.

Instead of attempting to identify and measure all the scattering processes we intend to quantify the affects of scattering guided by how it impacts the interpretation of the SNO data. Any light scattering will cause pmt hits to be out-of-time and out-of-position in a non-random way (unlike noise hits). A pattern recognition fitter wants to know how out-of-time and how out-of-position the hits are; knowing a total scattering cross-section is much less

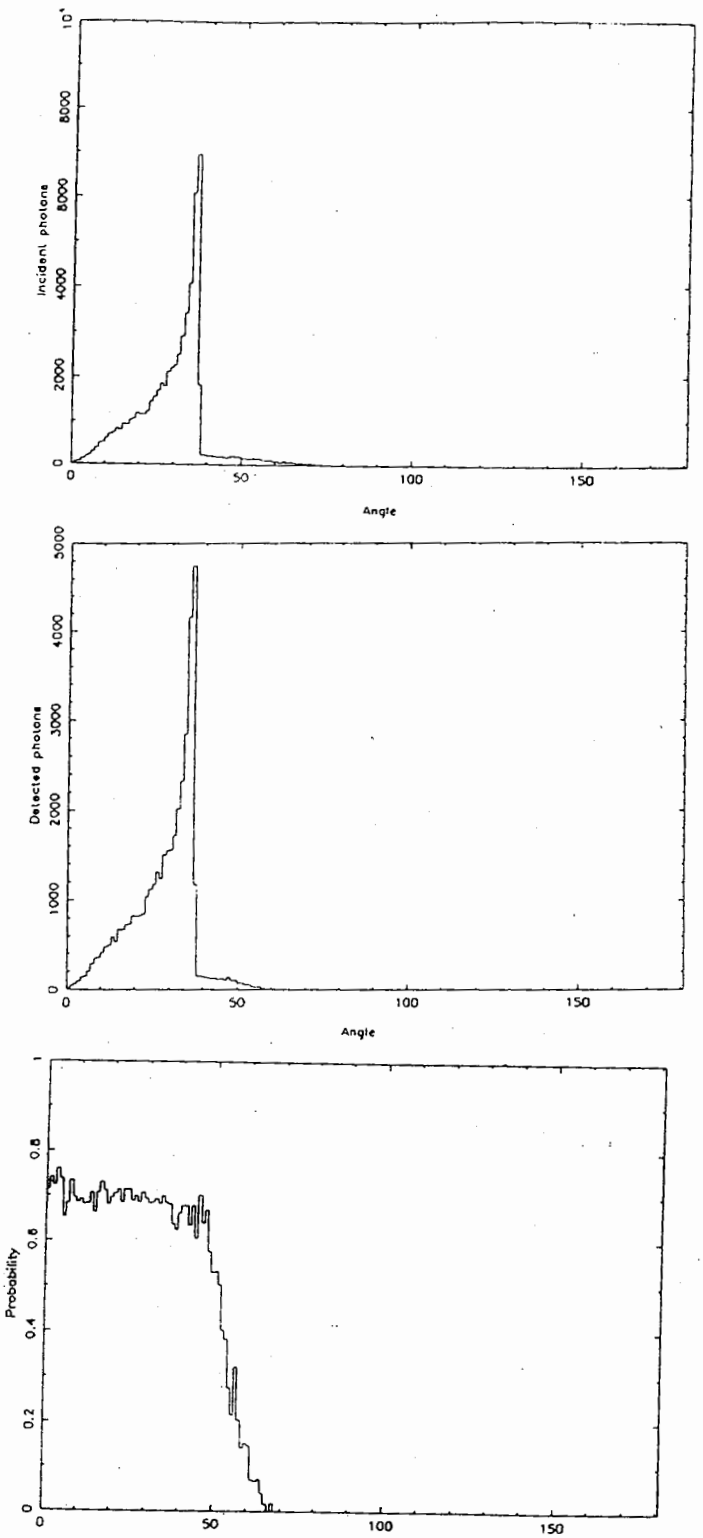

Figure 18: The top plot is the angular distribution of incident photons at each pmt in QMC for the laserball at (0,0,-500). The second plot is the angular distribution of detected photons. The third plot is proportional to the ratio which is the pmt response.

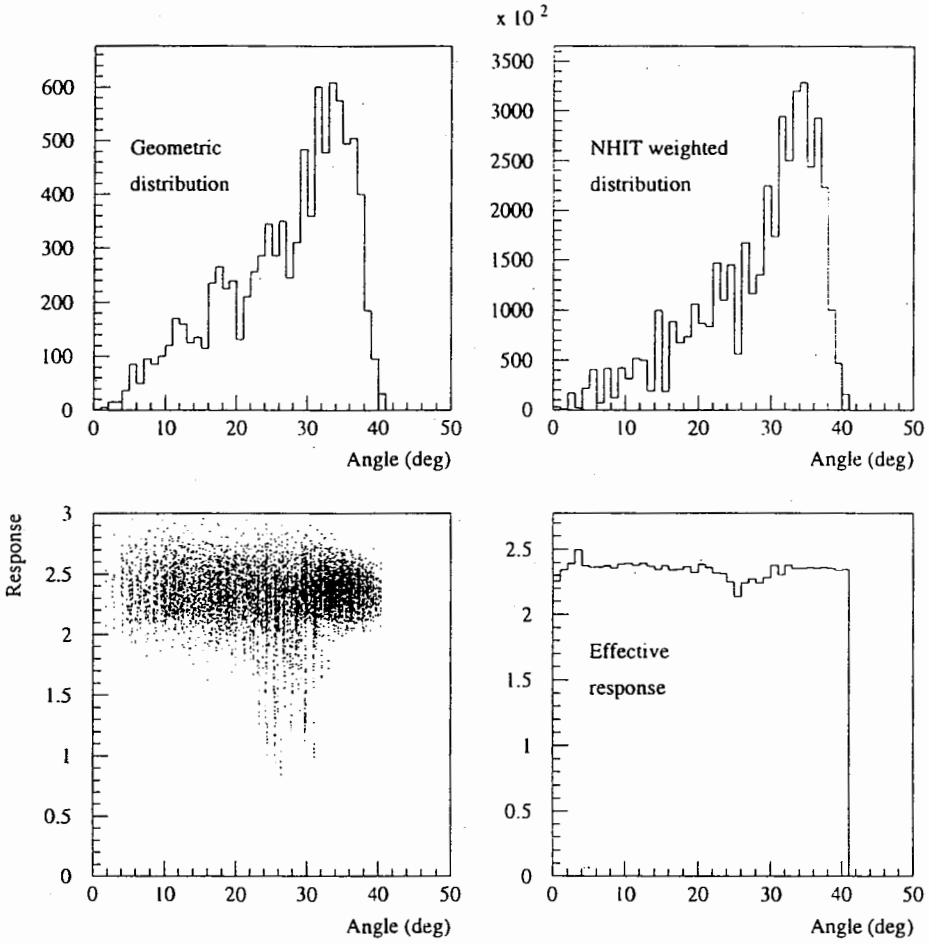

Figure 19: (a) Plot of the angular distribution for the line of sight to each pmt in SNOMAN from a point at (0,0,-500). (b) The angular distribution weight by NHIT. (c) Calculated pmt response by dividing out the attenuations and solid angle. (d) Effective pmt response by making a weighted histogram from plot (c) and dividing out the geometric distribution (plot a).

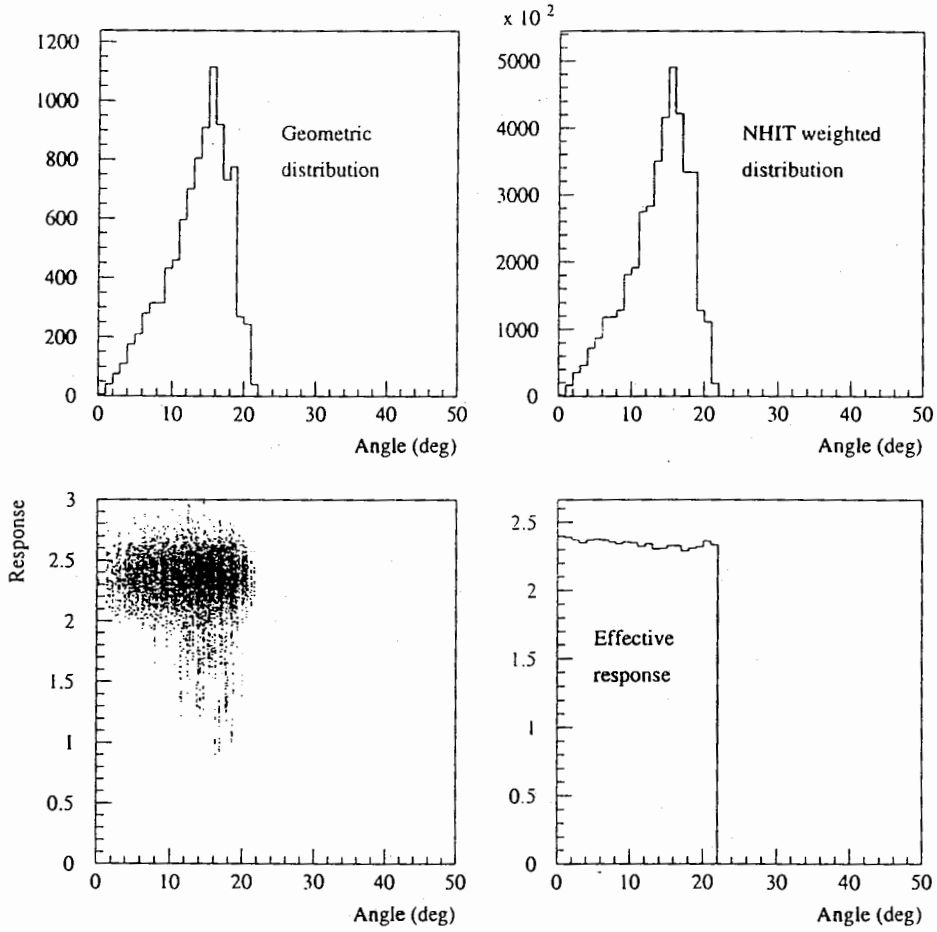

Figure 20: (a) Plot of the angular distribution for the line of sight to each pmt in SNOMAN from a point at (0,0,-250). (b) The angular distribution weight by NHIT. (c) Calculated pmt response by dividing out the attenuations and solid angle. (d) Effective pmt response by making a weighted histogram from plot (c) and dividing out the geometric distribution (plot a).

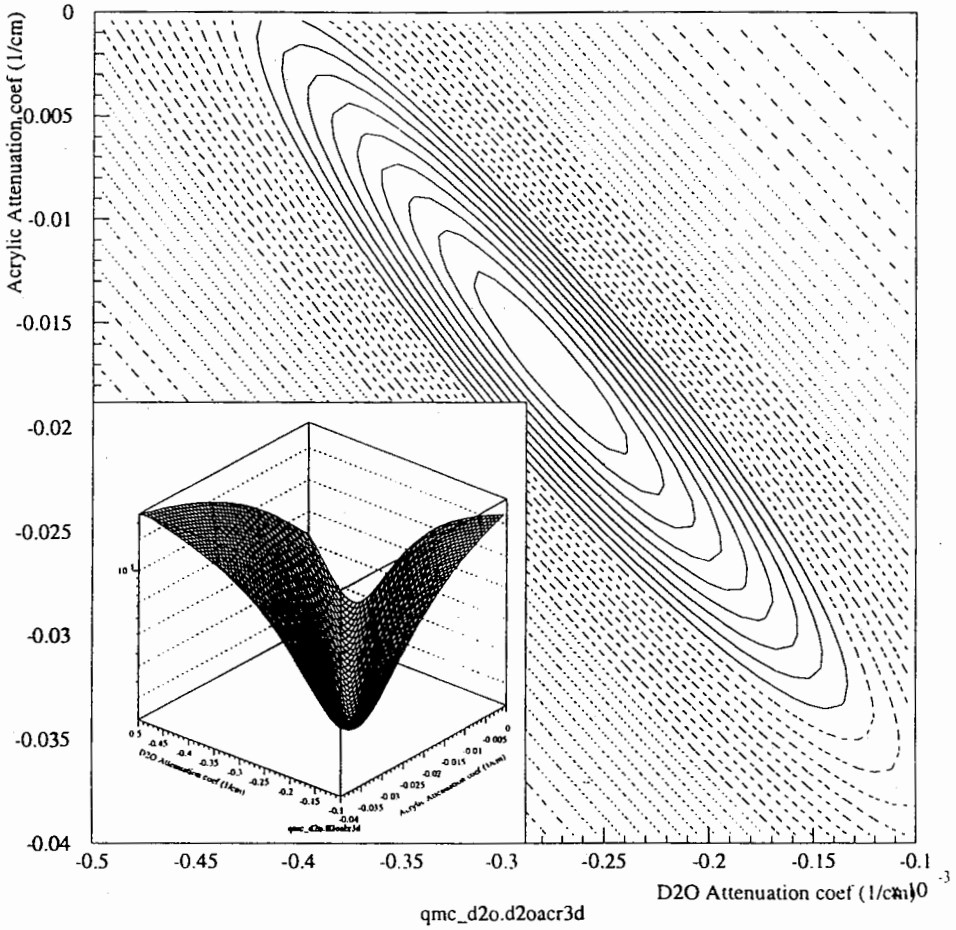

Figure 21: Chi-squared over variations in D_2O attenuation and acrylic attenuation from QMC data for five laserball positions in the D_2O. Best fit yields -0.000284 for D_2O (35m) and -0.0172 for acrylic (58cm).

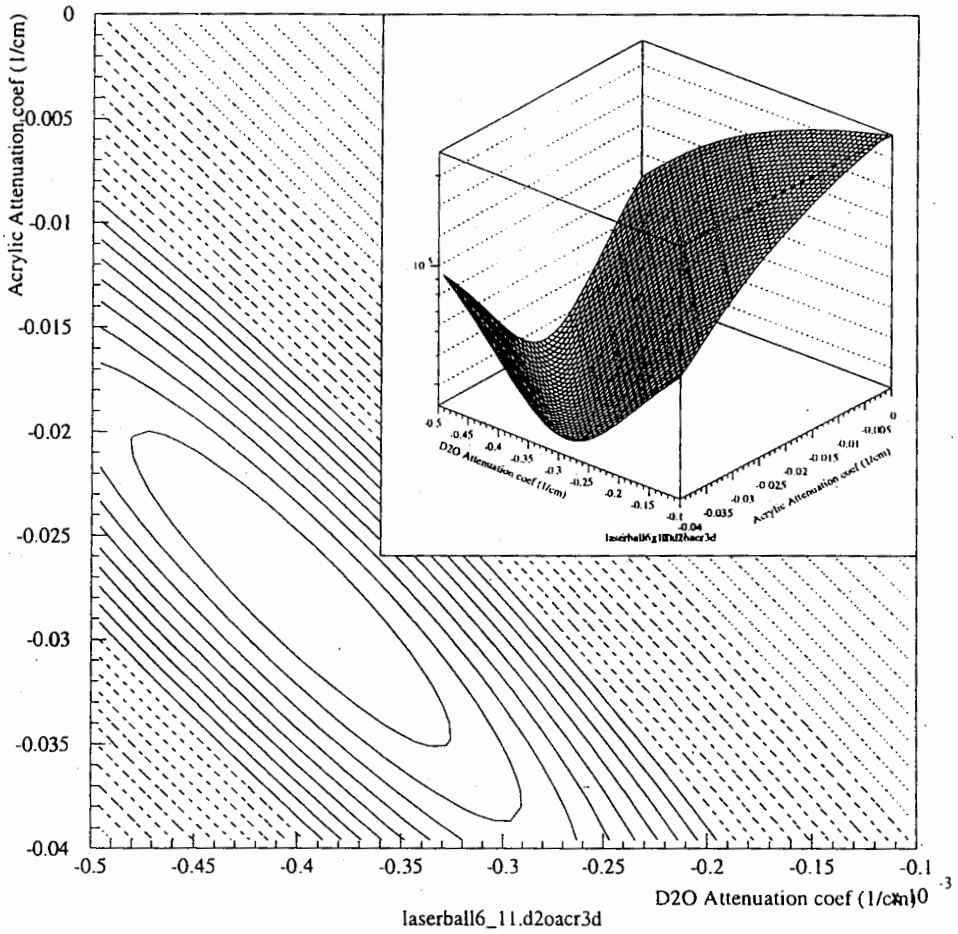

Figure 22: Chi-squared over variations in D_2O attenuation and acrylic attenuation from SNOMAN data for five laserball positions in the D_2O. Best fit yields -0.000406 for D_2O (25m) and -0.0280 for acrylic (36cm).

useful.

We intend to quantify bulk scattering in SNO with several parameterizations. Working from the time histograms we concentrate on the height and shape of the hits in set time windows following the prompt light. From this we can define an effective scattering cross-section. This cross-section will be smaller than the real cross-section as it will ignore forward scattered light. This is sensible as the SNO data cannot distinguish forward scattered or phase shifted light. The shape of the time distribution, parameterized by the slope at the window midpoint can indicate the broad nature of the angular distributions. Again this is reasonable as there will never be enough detector event data to be sensitive to any fine structure of coherent scattering angular distributions.

It is possible, and it is planned, in SNO to study scattering distributions using a directed light source. In this report I discuss only scattering with an isotropic source, as this data will be embedded within the calibration histograms.

There are three modes of scattering to be considered: dipole (Rayleigh) scattering, Mie scattering and scattering from larger particulate matter. Rayleigh scattering is due to thermally fluctuating electron densities; it is expected to dominate due to the wide $(1 + \cos^2\theta)$ angular distribution.

Mie scattering is the intermediate case where the size of the scattering centre is similar to the photon wavelength. The angular distributions must be worked out more rigorously due to phase coherences. The effect is to produce angular distributions that are very forward peaked, so that in the SNO detector the result is better characterized as an absorption.

Any larger particulate matter suspended in the water will absorb and reflect light. Assuming a spherical shape of radius a, the reflected light is uniform

$$\frac{dN}{d\Omega} = \frac{a^2}{4} \tag{8}$$

Since the distributions will be indistinguishable, I combine specular reflection with Rayleigh scattering by considering the distribution

$$\frac{dN}{d\Omega} = 1 + k\cos^2(\theta) \tag{9}$$

where $0 \leq k \leq 1$.

I study each of these scattering processes in the follow sections. The conclusion is that for the purposes of energy calibration and fitters all bulk scattering can be characterized by a single *effective* scattering length and absorption length.

7.1 Dipole and Specular Scattering

To study the effects of scattering I start with dipole (Rayleigh) scattering, then try varying distributions keeping with the same general form. For the predicted water purity levels then Rayleigh scattering will be the dominant process. For an optical source at the centre of the detector there is a time period of about 40 nsec where there can be no real tube hits unless the photon has made a large angle scatter from within the bulk medium. This suggests an opportunity for determining a characteristic scattering length for dipole scattering in water. The experimental data is unreliable in this area, but since dipole scattering is due to variations in electron density then the scattering should be the same in D_2O and H_2O.

Averaged over polarisations the dipole polar angular distribution has a $(1 + \cos^2\theta)$ shape. To permit an admixture of bulk specular scattering I take the distribution $(1 + k\cos^2\theta)$. Including absorption and transforming the angles into time one finds, for the laserball at the centre of a homogeneous detector, the time spectrum for photons undergoing a single Rayleigh scattering event is

$$\frac{dN}{dt} = \frac{3N_o}{2(k+3)x_s}\exp\left(-\frac{vt}{x_a}-\frac{vt}{s_s}\right)\int_0^R\left[\left(1+k\left\{\frac{v^2t^2+x^2-R^2}{2vtx}\right\}^2\right)\right.$$
$$\left.\times\left(\frac{v^2t^2+R^2-x^2}{2xvt^2}\right)\exp\left(-\frac{x}{x_a}-\frac{x}{x_s}\right)\epsilon(\cos\alpha)\right]dx \qquad (10)$$

where $\epsilon(\cos\alpha)$ is the pmt efficiency and angular response with

$$\cos\alpha = \frac{R^2+v^2t^2-x^2}{2vtR}. \qquad (11)$$

The absorption and scattering lengths are given by x_a and x_s. Figure (23) shows the results of a computation, where the integral was split into the D_2O and the H_2O regions and integrated across the detector several times.

Terms were included for specular reflection off the pmts, re-transit across the detector and multiple scatters. The spectrum has unphysical sharp secondary peaks since the calculation assumes that all reflected light bounces back from the pmts at 180°. I use this time distribution in all subsequent analyses since generating these data in the full Monte Carlo (SNOMAN) would take several CPU-weeks.

I now chose a window from 45 to 65 nsec and integrate the number of counts for calculated time spectra using a range of D_2O absorption lengths and scattering lengths. A 3D map of this integral versus the absorption length and scattering length is shown in figure 24 for $k = 0$ and $k = 1$. The calculation was done also for other k values but are not shown as these are consistent with figure 24. We see that for reasonable values of the absorption length (about 60m) the 45-65 nsec integral is fairly independent of the absorption and k. Thus for all manor of dipole and specular scattering the *effective* scattering length is easily parameterized by the 45-65 nsec integral.

7.2 Non-dipole Scattering

I now turn to the intermediate case where scattering is from foreign impurities in the water of a size comparable to the wavelength of light. This is known as Mie scattering. The problem rapidly becomes intractable unless some simplifying assumptions are made about the scattering object shape and composition. Waltham [10] considered scattering from the bacteria *E.coli* whose refractive index was measured to be $n_b = 1.415$. He found that the total scattering cross-sections calculated for an ellipsoidal shape agreed with measurements.

I now calculate the angular distributions for *E.coli* and then determine the hit time distribution in SNO for an isotropic source at the centre of the detector. The light intensity a distance r away from a scattering centre is

$$I = I_o \frac{|S_1(\theta)|^2 + |S_2(\theta)|^2}{2k^2r^2} \tag{12}$$

where $k = 2\pi n_w/\lambda$ and

$$S_1(\theta) = \sum_{n=1}^{\infty} \frac{2n+1}{n(n+1)} \{a_n \pi_n(cos\theta) + b_n \tau_n(cos\theta)\}$$

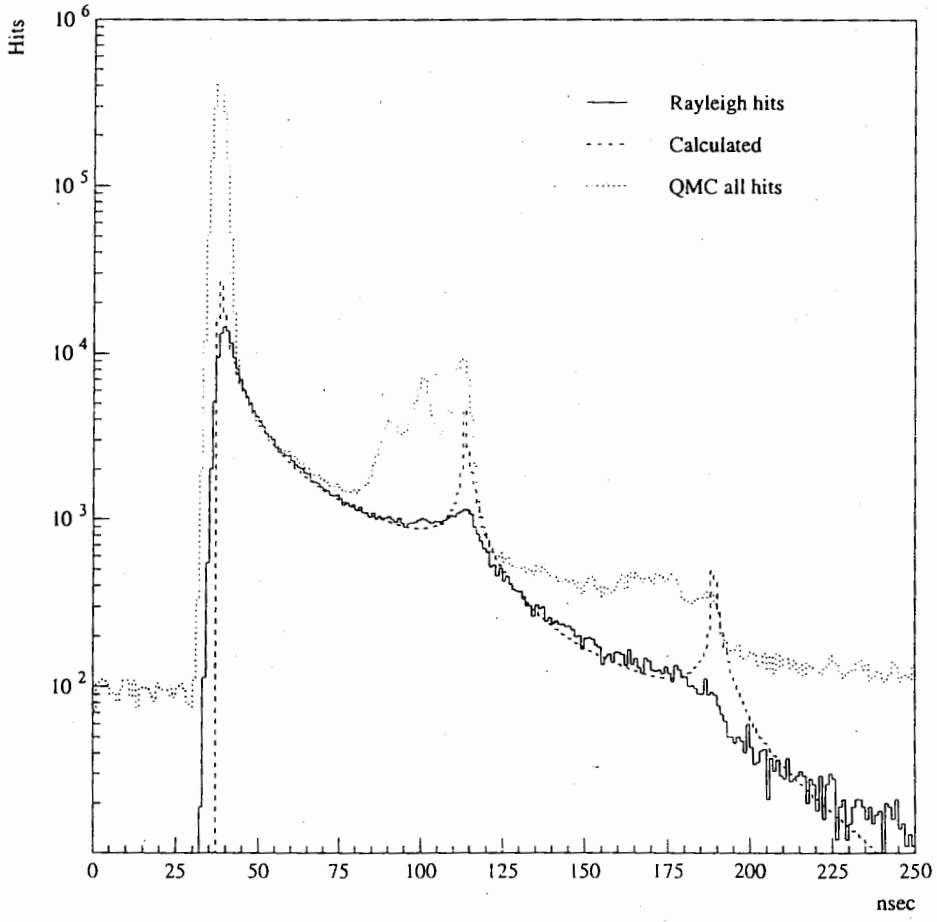

Figure 23: Comparison of simple calculated time spectrum to Monte Carlo data (QMC).

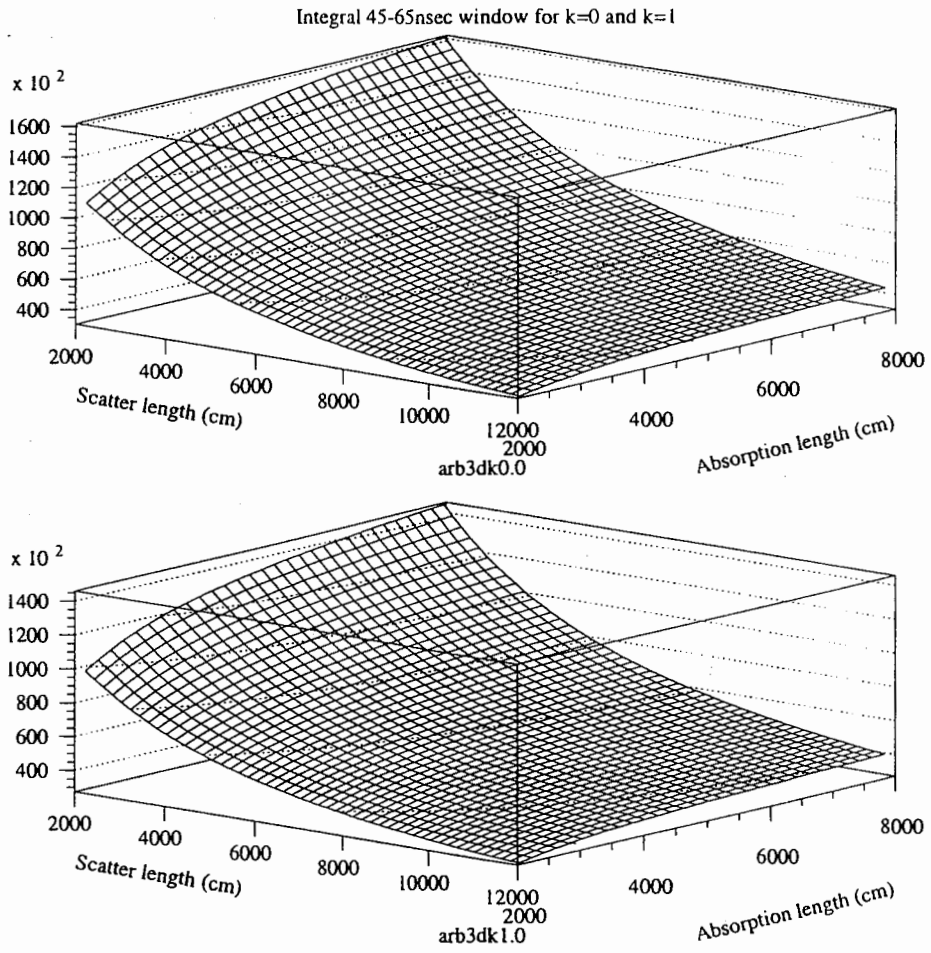

Figure 24: Integral of the 45-65 nsec window as a function of scattering length and absorption length for the distribution $1 + k\cos^2(\theta)$. For the upper plot $k = 0$ and for the lower plot $k = 1$. We see that the integral can be specified by a effective scattering length and is fairly independent of k and the absorption.

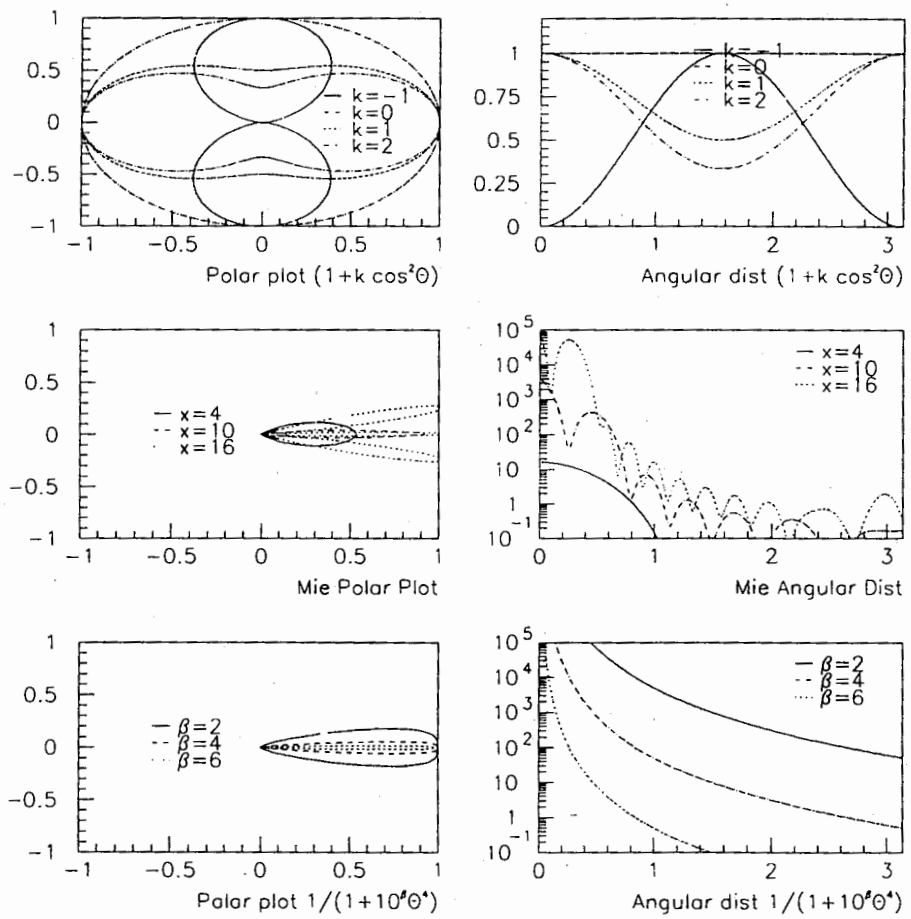

Figure 25: The top plots show the polar and angular distribution for dipole-like scattering. The middle plots show the distribution calculated from Mie theory for several aspect ratios. The lower plots shows a simple model for Mie type scattering distributions.

$$S_2(\theta) = \sum_{n=1}^{\infty} \frac{2n+1}{n(n+1)} \{b_n \pi_n(cos\theta) + a_n \tau_n(cos\theta)\} \quad (13)$$

The Mie functions (π_n, τ_n) and coefficients ($a_n(x)$, $b_n(x)$) can be found in[11] and are functions of the aspect ratio $x = ka$ with a the particle radius. Some angular distributions are plotted in figure 25 for the range of aspect ratios of interest ($x = 4$ to $x = 16$).

Similar to equation 10 the time distribution is

$$\frac{dN}{dt} = \frac{2\pi N_o R t \epsilon}{\langle f(\theta) \rangle x_s} \exp\left(-\frac{vt}{x_a} - \frac{vt}{s_s}\right) \int_0^R \left[f\left(\cos^{-1}\left\{\frac{R^2 - v^2t^2 - x^2}{2vtx}\right\}\right) \times \left(\frac{v^2t^2 + R^2 - x^2}{2xRvt^2}\right)^2 \exp\left(-\frac{x}{x_a} - \frac{x}{x_s}\right)\right] x\, dx \quad (14)$$

where the pmt angular response has been approximated by $\cos\alpha$. The angular function f is given by

$$f(\theta) = |S_1(\theta)|^2 + |S_2(\theta)|^2 \quad (15)$$

but was actually replaced by a Chebyshev polynomial fit to the distributions. As before, equation 14 was integrated to produce a time spectrum including terms for reflection off the pmts. Again the counts in the 45 to 65 nsec window are summed. These results are shown in figure 26, where the integral counts in the 45-65 nsec window is plotted as a function of the scattering particle aspect ratio. In the first case the scattering length is held fixed at $x_s = 6666$cm; we see clearly that the time distribution is insensitive to the aspect ratio (and hence insensitive to the details of the angular distribution). In the second case the bacterial density[4] is held fixed at 8524cm^{-3} and the scattering cross-section is calculated from the Mie formula. The integral is linearly dependent on the aspect ratio, hence the time distribution is well characterized by a single parameter: the scattering length. That is, whether any change in scattering length is due to a change in particle (bacteria) size or a change in the bacterial density does not matter. It can noted that the bacterial density used here 8524cm^{-3} is very high, yet still the resulting time

[4]I picked the value for the density at 8524cm^{-3} because it worked out to the same scattering length used in QMC for Rayleigh scattering for $x = 10$ at 386nm.

distribution integral is down by about an order of magnitude from Rayleigh scattering.

To investigate the sensitivity to the forward peaks in the angular distributions I replaced f with a simple form with a forward peak parameterized by β (see figure 25)

$$f(\theta) = \frac{1}{1 + 10^{\beta}\theta^4} \tag{16}$$

Again calculating time distributions and integrating the 45-65 nsec window the results are seen in figure 27. I plot the 45-65 nsec window as a function of the parameter β. We see that when β is negative we essentially have Rayleigh scattering. As β gets to a value of 2 the distribution is becoming forward peaked as in Mie scattering and the integral drops rapidly. For β larger than 2 the integral is constant with a value just the same as for Mie scattering with the same scattering length.

I conclude here that the SNO detector is sensitive only to wide angle scattering like Rayleigh or specular scattering and that this scattering can be parameterized by a single effective scattering length. Scattering then can always be assumed to be uniform with an *effective* scattering length given by the integral of the time histogram between 45 and 65 nsec. Mie scattering has a very minor effect due to the strong forward peak of the angular distribution. In fact SNO can tolerate bacterial counts an order of magnitude higher than Waltham's initial estimates [10] (10^5 L^{-1}) while still being below Rayleigh scattering. High bacterial counts will just add to the effective scattering length while the light distribution within the detector will still be well modeled by a uniform distribution with this *effective* scattering length.

8 PMT reflectors

In figure (10a) for a laserball at the centre we see there are several peaks in the spectrum associated with reflections off the pmts; in SNOMAN there at are peaks at 96.8 and 113.3 nsec and in QMC at 91.5, 99.5 and 113.3 nsec. To explain these we consider the distances and reflection angles that would correspond to these peaks as a transit time offset. The peaks at 113.3 nsec are clearly direct reflections equivalent to a triple radius transit. Taking the photon path to be a detector radius plus a PSUP cord, one finds the pmt

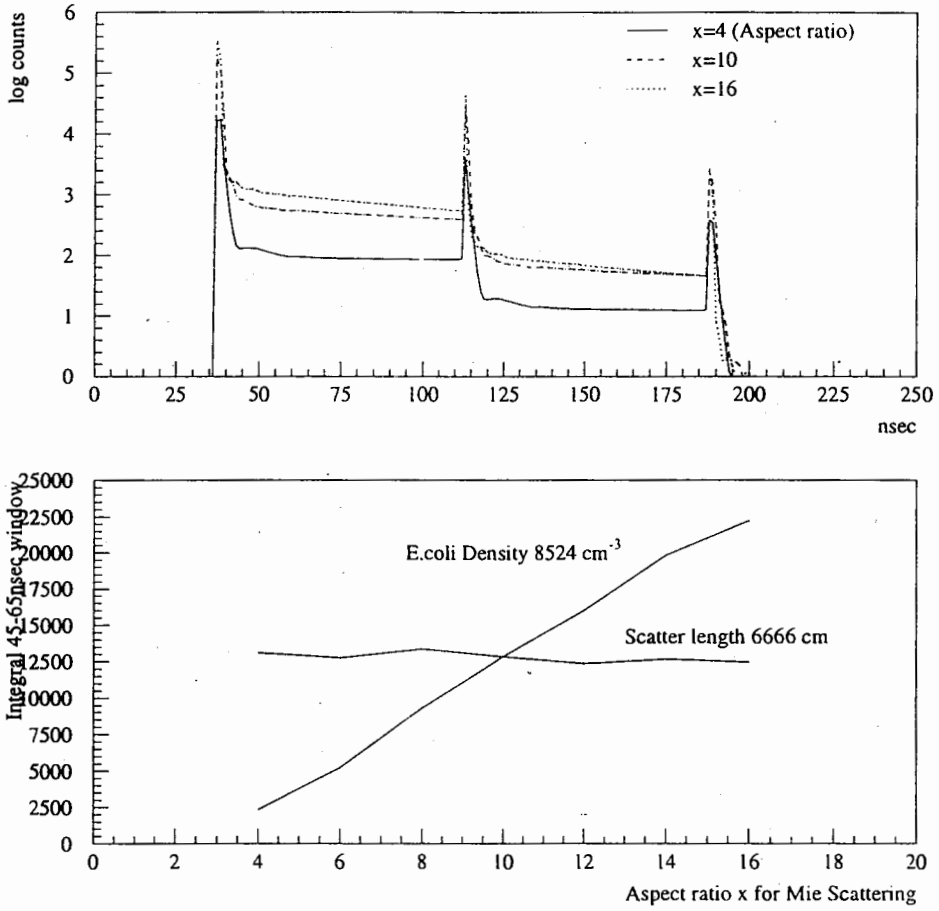

Figure 26: The upper plot is the time distribution for Mie scattering with various aspect ratios. The lower plot show the counts in the 45-65 nsec window versus the aspect ratio in Mie scattering for (a) constant density with the scattering length worked out from the aspect ratio, and (b) constant scattering length.

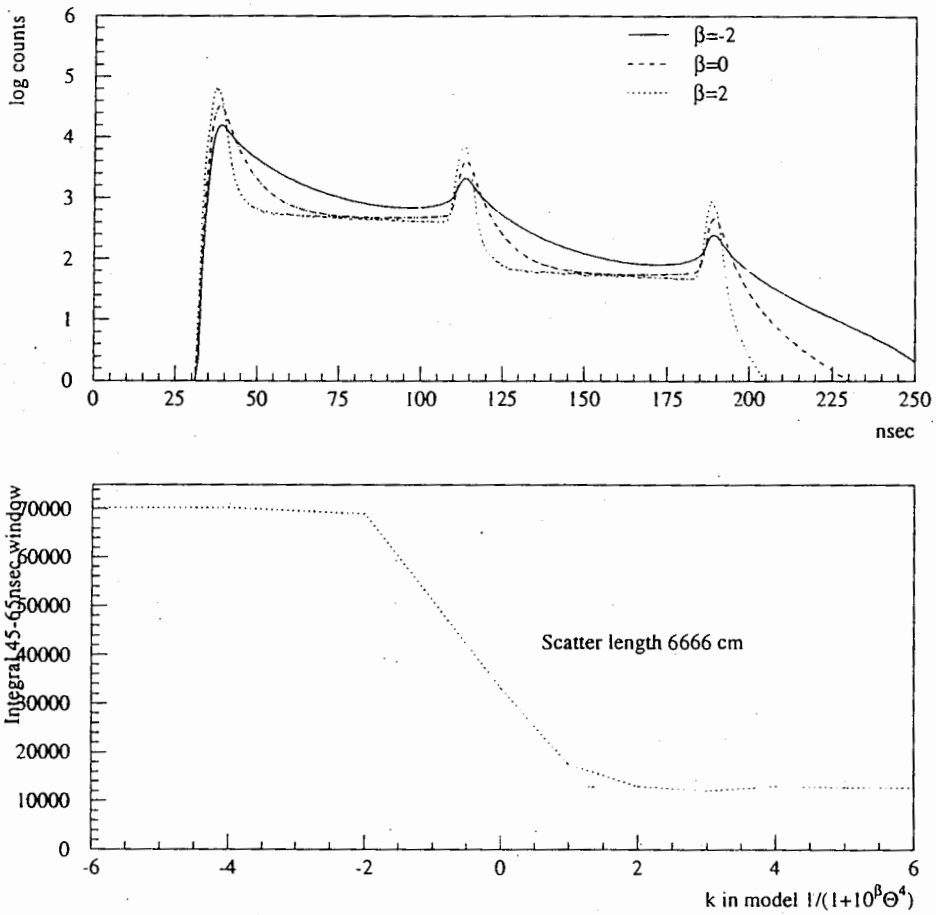

Figure 27: The upper plot is the time distribution for the scattering model $1/(1 + 10^{\beta}\theta^4)$ with several values of β. The lower plot shows the counts in the 45-65 nsec window versus β.

reflection angle to be given by

$$\cos(\theta) = 0.01336\,t - 0.5 \tag{17}$$

Thus for SNOMAN there is a prominent reflection at about 37° while QMC has pmt reflections at 44° and 34°. A strong shoulder on the 37° peak in SNOMAN suggests it may have an enhanced reflection at about 47°. These peaks at roughly 35° and 45° must be due to light photocathode-reflector interactions that happen to be enhanced at these angles.

Tracing possible ray paths for the pmt-reflector combination I find that the wide 45° reflection requires a large angle (approx 50°) reflection from the photocathode. This is perhaps not so surprising since it is well known [8] that the photocathode reflection coefficient rises dramatically at 50° for the parallel polarisation. Since this reflection is near the bucket cutoff then the slightly different reflector shapes for SNOMAN and QMC might explain why the peak is only prominent in QMC.

The peak at 35° has no similar explanation and must be due to a more subtle geometry arrangement. As an experimental curiosity I positioned a SNO pmt/reflector unit on a bench pointed toward a wall at a distance of 230cm. Shining a beam flash light toward the pmt and along the axis produced reflections projected on to the wall. A sharp image of the reflector petals was observed in a ring with 165cm radius on the wall; corresponding to a reflection angle of 35.5°. It was quite surprising that the non-imaging reflectors when combined with the photocathode do produce an image at a certain angle and that this image was predicted by the Monte Carlo. This is a good boost of confidence for the pmt model since this reflection had not been noticed before it was uncovered in Monte Carlo data.

To reflect off at 35°, the photons must bounce only once off both the photocathode and the omega reflector. The number of hits under the 35° peak relative to the prompt peak provide a good way of making a global evaluation of the omega reflectivity. As a quick evaluation of this proposal I ran SMOMAN several times with a reduced value for the omega reflectivity coefficient. Figure 28 is a plot of the ratio of the 35° peak to prompt peak. This ratio is actually a bit complicated since both the reflecting and the hit pmt has a dependence on the reflector. The approximation here is that the 35° peak varies with the coefficient squared, while the prompt peak is partially linearly dependent on the reflection coefficient. It seems like it

would be straight forward to track the integrated reflector condition from this ratio. Note that this ratio would also have a dependence on the D_2O attenuation length that should be accounted for.

9 On-going and Future Work

In this report I have attempted to present the methodology that is being developed for the optical calibration. This report is meant to provide the background for future reports on specific analysis. Specifically I have not included in this report the fitting for the acrylic panel-by-panel or an uncertainty analysis.

The software routines are now under construction to perform a complete optical fit with uncertainty analysis. The final stage of this analysis is then to construct and test a detector response function $E_e = E(\text{nhit}, R_{\text{fit}}, \theta_{\text{fit}})$ based on the fitted optical constants.

SNOMAN requires changes to permit variations in transmission in acrylic from panel to panel and variations in individual pmts (eg. the QE's distributed according to [12]).

Further changes are also being made to the optical hardware, including development of a shortwave length source and directional/multi-directional fittings for the laserball. I am also developing a driver circuit for a double heterostructure UV diode. These will be described in [2].

References

[1] S. Biller and R.J. Ford *Optical Calibration*, SNO-STR-97-0XX (1996).

[2] R.J. Ford *Description of the SNO N_2/Dye Laser Optical Calibration Source*, SNO-STR-96-056 (1997, still in progress).

[3] A.L. Hallin *Calibration Devices Above Deck*, Queen's (1996).

[4] B.A. Robertson *Review of SNO Calibration*, SNO-STR-96-036 (1996).

[5] T.J. Radcliffe *Optics and Geometry in the SNO Detector*, SNO-STR-95-007 (1995).

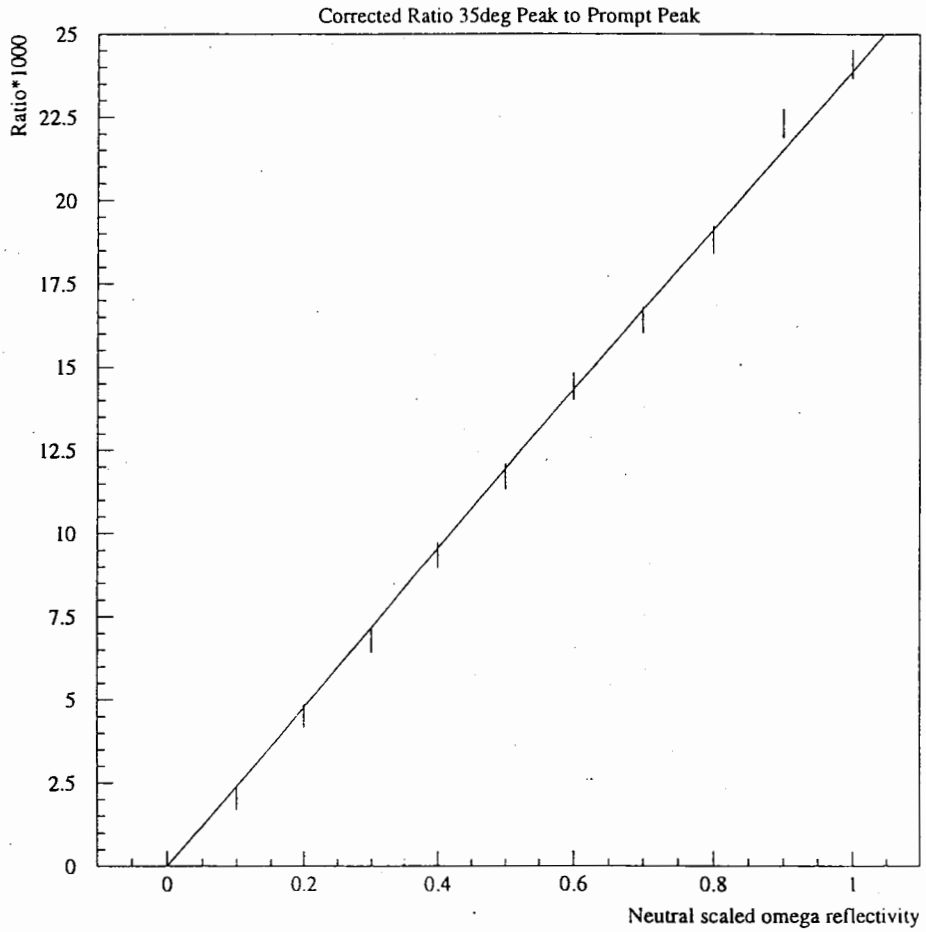

Figure 28: Corrected ratio of hits in the 35° peak to the prompt peak plotted versus the pmt omega reflectivity.

[6] A.L. Hallin *Calibration Issues and Plan*, Queen's (1993).

[7] G.T. Ewan *et al. Sudbury Neutrino Observatory Proposal*, SNO-STR-87-12 (1987).

[8] M.E. Moorhead, N.W. Tanner and A.P. Ferraris *Reflections from a Bialkali Photocathode*, Oxford (1988).

[9] M.D. Lay *Creation and Detection of Cherenkov Light in the Sudbury Neutrino Observatory*, PhD. Thesis, Oxford (1994).

[10] C. Waltham *et al.* Appl. Opt. **33** 31 (1994) 7536.

[11] H.C. van de Hulst *Light Scattering by Small Particles*, Dover, New York (1981).

[12] C.J. Jillings *et al.* NIM A 373 (1996) 421-429.